

東京大学大学院新領域創成科学研究科
基盤科学研究系
先端エネルギー工学専攻

2004 年度修士論文

Study on Plasma Characteristics
of Electron Cyclotron Heating Experiments
in the Internal Coil Device Mini-RT
内部導体装置 Mini-RT の
電子サイクロトロン加熱実験における
プラズマ特性に関する研究

学籍番号 36205
氏名 後藤 拓也
指導教員 小川 雄一 教授

(2005 年 2 月 14 日提出)

Contents

1	Introduction	1
1.1	Plasma and Fusion	1
1.2	Internal Coil Devices and the Mini-RT Program	2
1.3	Motivation and Objective of the Study	4
2	Outline of the Internal Coil Device Mini-RT	6
2.1	Specification of Mini-RT	6
2.2	Operational Flow	7
3	Experimental Setup	13
3.1	Electrostatic Probe	13
3.1.1	Double Probe	14
3.1.2	Triple Probe	17
3.2	Microwave Interferometer	20
3.3	Plasma Production System	25
3.4	Setup of the Measurement Tools	25
4	Experimental Results	29
4.1	Experiments with Supported Internal Coil	29
4.2	Experiments with Levitated Internal Coil	38
4.3	Experiments of X-mode Wave Injection	48

5	ECH Plasma Properties	51
5.1	Physics of Electron Cyclotron Heating	51
5.1.1	Resonant Condition	51
5.1.2	Absorption Coefficient	56
5.2	Over-dense Plasma Production by Using Electron Bernstein Waves	60
5.2.1	Property of Electron Bernstein Waves	60
5.2.2	Mode Conversion to EBW from Electromagnetic Waves . . .	61
5.2.3	Application of EBW on Mini-RT experiments	65
6	Conclusion	69
A	Sheath Theory	72
B	High Energy Electron Loss by the Support Structure	76

List of Figures

2.1	Cross-sectional view of the Mini-RT device	7
2.2	Photograph of the Mini-RT device	8
2.3	PCS temperature and current variations in excitation	10
2.4	Picture of the levitated internal coil	10
2.5	Typical magnetic configuration of the Mini-RT device	11
2.6	Displacement of the internal coil in the test operation	12
3.1	Typical current-voltage characteristics measured with a double probe	14
3.2	Drawing of the double probe	16
3.3	Schematic drawing of circuit diagram used in double probe measure- ment	16
3.4	Method for estimation of the ion saturation current	17
3.5	Schematic circuit diagram of a triple probe	17
3.6	Schematic drawing of circuit diagram used in triple probe measurement	19
3.7	Schematic circuit diagram of the microwave interferometer	24
3.8	Photograph of the 2.45GHz ECH system	26
3.9	Location of the measurement system	27
3.10	Photograph of the lens horn antenna	28
3.11	Setup of the lens horn antenna	28
4.1	Photograph of the plasma with supported internal coil	30

4.2	Magnetic configuration with the supported internal coil	30
4.3	Electron density profile measured by double probe	31
4.4	Electron temperature profile measured by double probe	32
4.5	Comparison of line-averaged electron density	33
4.6	Calculation method of line-averaged density	34
4.7	ECH power dependence of electron density measured by double probe	35
4.8	ECH power dependence of electron temperature measured by triple probe	35
4.9	ECH power dependence of electron density measured by triple probe	36
4.10	ECH power dependence of electron temperature measured by triple probe	36
4.11	ECH power dependence of line-averaged electron density	37
4.12	Magnetic configuration with levitated internal coil	39
4.13	Photograph of the plasma with levitated internal coil	40
4.14	Neutral pressure dependence of electron density	41
4.15	Neutral pressure dependence of electron temperature	42
4.16	Relation between coil-support gap and electron density	42
4.17	Relation between coil-support gap and line-averaged electron density	43
4.18	Electron density profile measured by triple probe	45
4.19	Electron temperature profile measured by triple probe	45
4.20	The calculated shape of LCFS	46
4.21	Electron density decay with supported internal coil	47
4.22	Electron density decay with levitated internal coil	47
4.23	Electron density profile with X-mode injection	49
4.24	Electron temperature profile with X-mode injection	50
5.1	SX-B conversion mechanism	62
5.2	O-X-B conversion mechanism	63

5.3	FX-SX-B conversion mechanism	64
5.4	Calculated position of UHR and LHC in the experiment	68
A.1	Structure and potential profile of ion sheath	73
B.1	Total cross sections for the ionization of molecular hydrogen	78

Abstract

The Mini-RT device is an internal coil device which aims the demonstration of the extremely high beta plasma confinement predicted in the two fluid relaxation theory proposed by Mahajan and Yoshida. Through the first plasma experiment, energizing test and levitation control test of the internal coil, the Mini-RT project is now in the phase that plasma experiment with levitated internal coil is practicable. In this study, several experiments have been carried out in order to comprehend the properties of the plasma with levitated internal coil, and the physics approach for the high-density/high-temperature plasma production has been investigated. In these experiments, plasma has been produced by electron cyclotron heating (ECH) by using a 2.45GHz microwave. The measurement of plasma parameters has been carried out by the electrostatic probes and 75GHz microwave interferometer. Through the experiments, it becomes clear that the removal of supporting structure by the levitation of the internal coil enables plasma production with low neutral gas pressure (i.e. $< 1.0 \times 10^{-2}\text{Pa}$), which cannot be achieved when the internal coil is supported. In addition, both electron density and temperature are improved by the levitation. Especially, maximum electron density measured by electrostatic probes totally above the cutoff density of 2.45GHz microwave ($7.4 \times 10^{16}\text{m}^{-3}$). It indicates overdense plasma can be produced in the Mini-RT device. The ionization degree has been improved up to 50% according to the density increase. However, the absorption coefficient of incident microwave power is quite low ($\sim 2\%$ by rough estimation), and the collision of the electron with the neutral gas particle is still dominant. It is desired to achieve full ionization and further increase in the plasma temperature in near future so as to attain high beta plasma confinement. While it also becomes

clear that the Mini-RT device has the possibility of the mode-conversion from electromagnetic wave to electron Bernstein wave (EBW) with high efficiency ($\sim 65\%$) by its nature when the internal coil is levitated. The application of EBW on high efficient plasma heating in the Mini-RT device is expected.

Chapter 1

Introduction

1.1 Plasma and Fusion

Plasma is a kind of charged gas and sometimes described as fourth state of the matter. Although it can be seen under limited condition on the earth (e.g., aurora, lightning), when we look into the space, there are filled with various state of plasma, such as fixed star, solar wind, interstellar gas. It is said that they may make up 99% of the total matter in the space. So the elucidation of the plasma physics leads directly to the comprehension of the phenomena in the space. Then various study of plasma physics has been carried out in the field of astronomy and planetary science.

While recently, a variety of applications of the plasma physics on the engineering have been studied. One of these application is the development of nuclear fusion energy source, which expected to make a great contribution on the settlement of energy and environmental problem. It is indispensable to clarify the physics mechanism of plasma (e.g., motion, stability, relaxation) in order to achieve the implementation of these significant applications.

Strictly, plasma is defined as a quasi-neutral gas of charged and neutral particles which exhibits collective behavior [1]. Thus plasma simultaneously shows

particulate behavior as a charged particle and collective behavior as a neutral fluid. This characteristics makes the physics of plasma quite complicated. Especially, the physics of flowing plasma has not yet been clear.

1.2 Internal Coil Devices and the Mini-RT Program

In magnetic confinement fusion, major devices such as tokamak and helical confine plasma with strong, mainly toroidal field. So plasma is confined in a torus region enclosed by a conductor that generates toroidal magnetic field. While there are a configuration which uses dipole field generated by a circular current for plasma confinement just the same as the ionosphere plasma confined by the geomagnetic field. A device adopting this configuration is called for an internal conductor because in the case plasma is confined around the conductor. If a normal conductor is adopted for such internal conductor, inner structure (e.g., current feed, supporting structure) inevitably crosses the line of magnetic force around the conductor. It causes an energy loss of plasma and disable high temperature plasma confinement. In order to avoid this problem, the internal conductor need to be magnetically levitated by adopting a superconductor for its windings.

In fusion research, several internal conductor devices were constructed in mainly US and Europe in 1970s (e.g., Spherator, Levitron, Octapole). These devices adopted a low-temperature superconductor (e.g., NbZr, NbTi) and achieved position control with 0.1mm accuracy. The objective of these devices were to investigate electromagnetic feature of plasma (e.g, magnetic well, the effect of magnetic shear), and significant observation was carried out that leads the progress of MHD theory. However, all these internal conductor devices were shut down in the middle of 1970s due to the difficulty in the application of them to the fusion reactor system.

But internal conductor devices become to be highlighted again. Around 1980, several planetary explorer satellite including Voyager 2 found the extremely high beta plasma ($\beta \gtrsim 1$) in Jupiter's magnetosphere [2]. Beta value is defined as the ratio of plasma pressure and magnetic pressure as $\beta = \frac{p}{B^2/2\mu_0}$, and high beta means the possibility of high-temperature and high-density plasma confinement by relatively weak magnetic field. According to the fact that the beta value of present main fusion experimental devices are up to 10%, this discovery made a great impact on fusion science as giving perspective in downsize of a fusion reactor and implementation of advanced fusion used D-³He or p-B reaction which generates less radioactive waste than conventional D-T reaction.

Following these observations, intense studies have been carried out about the physics mechanism of keeping such high beta state. A. Hasegawa noted the fact that high beta confinement is realized by dipole magnetic field. He has developed a new relaxation theory and proposed a dipole field configuration with an internal coil [3]. In his theory the plasma relaxes to a high beta state under the constraints of the conservations of two adiabatic constants (μ and J). In order to demonstrate this concept, MIT/Columbia group has constructed a large-scale internal conductor device called as Levitating Dipole eXperiment (LDX) . While recent study on plasma physics has revealed the important role of flow in plasma. S. M. Mahajan and Z. Yoshida have discovered a new relaxation state based on two-fluid plasma theory [5]. They have predicted that plasma with strong flow may self-organized into stable macroscopic structures [4], and proposed a possibility of extremely high-beta plasma confinement. In order to study this self-organized state and demonstrate the high-beta plasma confinement, an internal conductor device is suitable because it can drive strong plasma flow by $\mathbf{E} \times \mathbf{B}$ drift with radial electric field. So the internal coil device called as RT(Ring Trap)-1 has been designed and under construction in Kashiwa campus, the University of Tokyo. Prior to this large scale experiments,

two devices have been developed. The one is a normal conductor device called as Proto-RT [6]. The experiments with the Proto-RT device have been bringing many significant discovery about the confinement of non-neutral plasma and the formation of radial electric field. And the other is a relative small, superconductor device called as Mini-RT, with which the experiments described in this paper have been carried out.

1.3 Motivation and Objective of the Study

Described in more detail in the next chapter, the feature of the Mini-RT device is that the internal coil can be magnetically levitated because of adopting a high temperature superconductor (HTS) for its windings. So the Mini-RT device enables plasma production in a dipole magnetic field without any interaction by the supporting structure. Up to now, several significant works have been successfully carried out in the Mini-RT program : plasma production with the supported internal coil, energizing test of the internal coil, stable levitation and position control of the internal coil, and plasma production with the levitated internal coil. The Mini-RT program is now in the phase that the plasma experiments with the levitated internal coil is practicable. It is expected that the levitation of the internal coil helps the improvement of the plasma parameters (e.g., electron density, electron temperature) because the support structure in the plasma region assumed to be a major obstacle. So confirmation of this assumption and the demonstration of the improvement of plasma parameters becomes to be an immediate subject prior to the final goal.

The objective of this study is the comprehension of plasma properties with the levitated internal coil and the investigation of the physics approach for improvement of plasma parameters. In order to achieve the objective, several experiments have

been carried out. Chapter 2 reviews the outline of the internal coil device Mini-RT. Chapter 3 describes the setup of the measurement and the plasma production system. Chapter 4 gives the results of the experiments. Related physics of electron cyclotron heating (ECH) is reviewed in Chapter 5. The conclusions is drawn in Chapter 6.

Chapter 2

Outline of the Internal Coil Device Mini-RT

All experiments and consideration in this paper have been carried out with the internal coil device Mini-RT. In this chapter, specification of the Mini-RT device and its operational flow are reviewed.

2.1 Specification of Mini-RT

Mini-RT is an internal coil device that has major radius of $R=0.5\text{m}$ and height of about 0.7m . Figure 2.1 shows the cross-sectional view of the Mini-RT device. The torus shape internal coil in the vacuum vessel generates dipole magnetic field like magnetosphere of planets. Figure 2.2 shows a photograph of the Mini-RT device.

The feature of the Mini-RT device is that the internal coil is wound with superconductor and can be magnetically levitated by the levitation coil located on the vacuum vessel. BSCCO-2223, one of a high-temperature superconductor (HTS), is adopted for the internal coil windings. At the present, the Mini-RT device is the unique device that using HTS for the internal conductor.

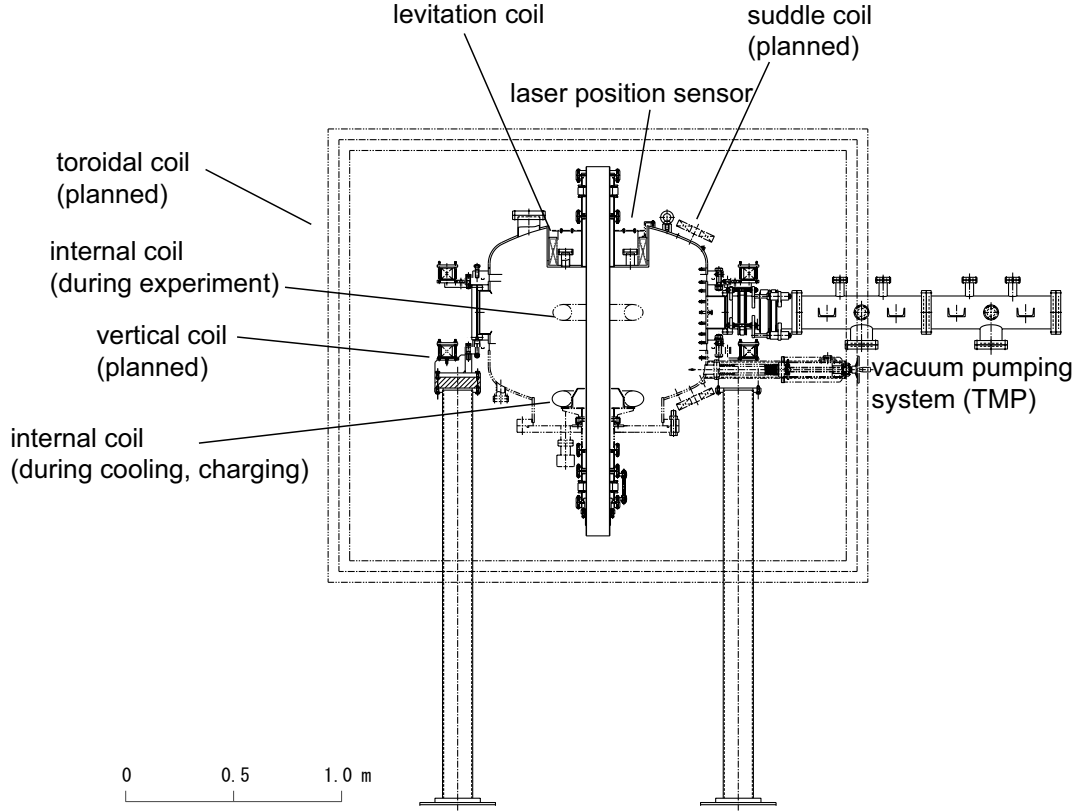


Figure 2.1: Cross-sectional view of the internal coil device Mini-RT. In this figure, the coil cooling and lifting system located under the vacuum vessel is not shown.

The major radius of the internal coil is 0.15m and the maximum coil current is 50kAturns. More detail specification of the Mini-RT device is given in Tab.2.1.

2.2 Operational Flow

Before holding an experiment, the internal conductor needs to be cooled for superconductive transition. Since HTS is adopted for internal conductor, required cooling temperature is just 20K and liquid helium is not needed. The internal coil is cooled at the bottom of the vacuum vessel directly by a helium gas generated



Figure 2.2: Photograph of the Mini-RT device.

with the GM refrigerator through the detachable transfer tubes.

When cooling is over, a current is charged to the internal coil directly by the external power supply through the detachable current feeds. So as to achieve persistent current mode during the coil floating phase, the persistent current switch (PCS) is build into the internal coil. During the current charge, the PCS is heated and its temperature is kept around 130K so as to hold the switch-off condition. When the coil current is increased up to the nominal value, the PCS is quickly cooled down and transited to the turn-on condition. Then the current of the power supply is gradually decreased, resulting in the replacement of the power supply current with the PCS one. Figure 2.3 shows the variations of PCS temperature T_{PCS} ,

Table 2.1: Specification of the Mini-RT device

major radius	0.5m
height	0.7m
major radius of the internal coil	0.15m
weight of the internal coil	16.8kg
conductor	BSCCO-2223 (HTS)
internal coil turn number	428
internal coil current	50kAturns (117A per turn)
stored energy of internal coil	598J
internal coil inductance	0.0876H
major radius of levitation coil	0.20875m
levitation coil turn number	68

current by the external power supply I_{shunt} , and current of the internal coil I_{Fcoil} .

After achieving persistent current mode, the internal coil separated from all connected components: transfer tubes, current feeds, and feed-through for measurement. Then the internal coil is lifted up by motor-driven supporting structure (which we call "lifter") to the equatorial plane of the vacuum vessel. In this state, the internal coil is levitated by applying current to the levitation coil. Figure 2.4 shows the picture of the levitated internal coil. Figure 2.5 shows the magnetic configuration of this condition. The position of the coil is detected by three laser displacement gauge, and stabilized by feed-back control of the levitation coil current. Figure 2.6 shows the displacement of the internal coil in the test operation. The position accuracy is less than $10\mu\text{m}$. In this state, lifter is downed till it is out of the plasma confinement region. Then plasma experiment is carried out. When the experiment is over, the floating coil is recovered by lifter and lifted down preparing for the next experiment.

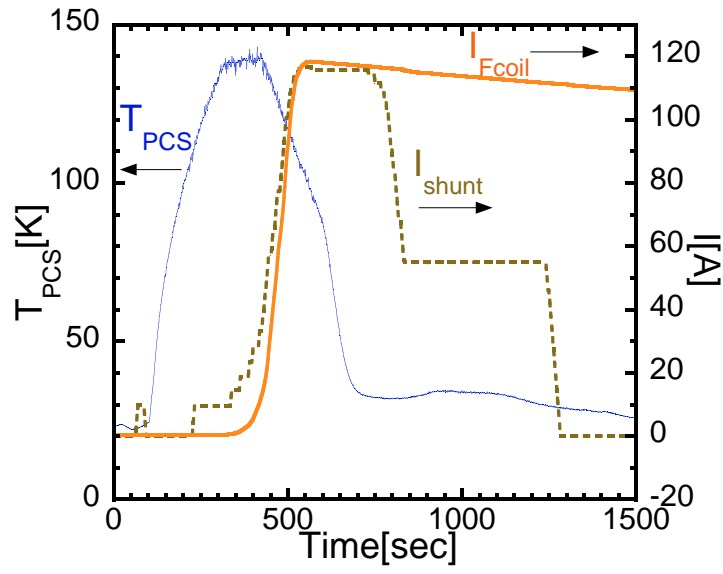


Figure 2.3: The variation of PCS temperature, current by the power supply, and current of the internal coil current in an excitation of the internal coil.



Figure 2.4: Picture of the levitated internal coil

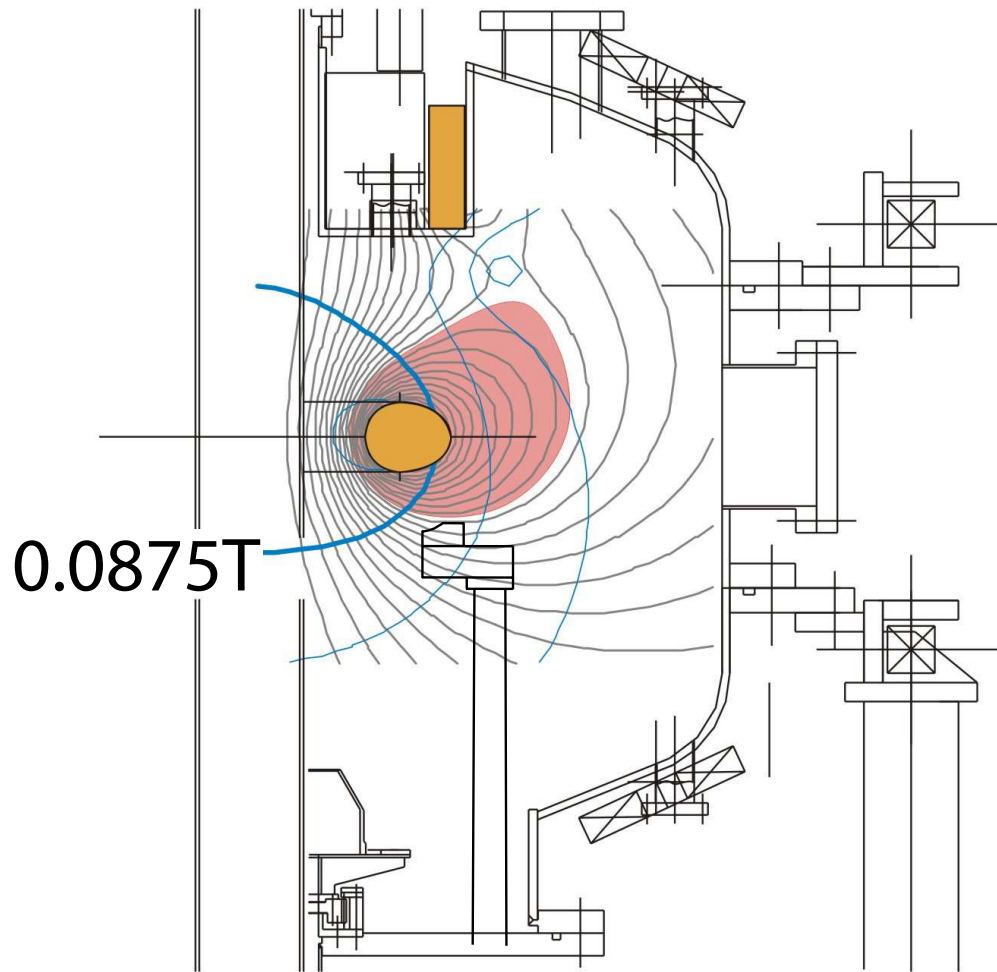


Figure 2.5: Typical magnetic configuration of the Mini-RT device. The currents of the internal coil and the levitation coil are 50kAturns and 15kAturns, respectively.

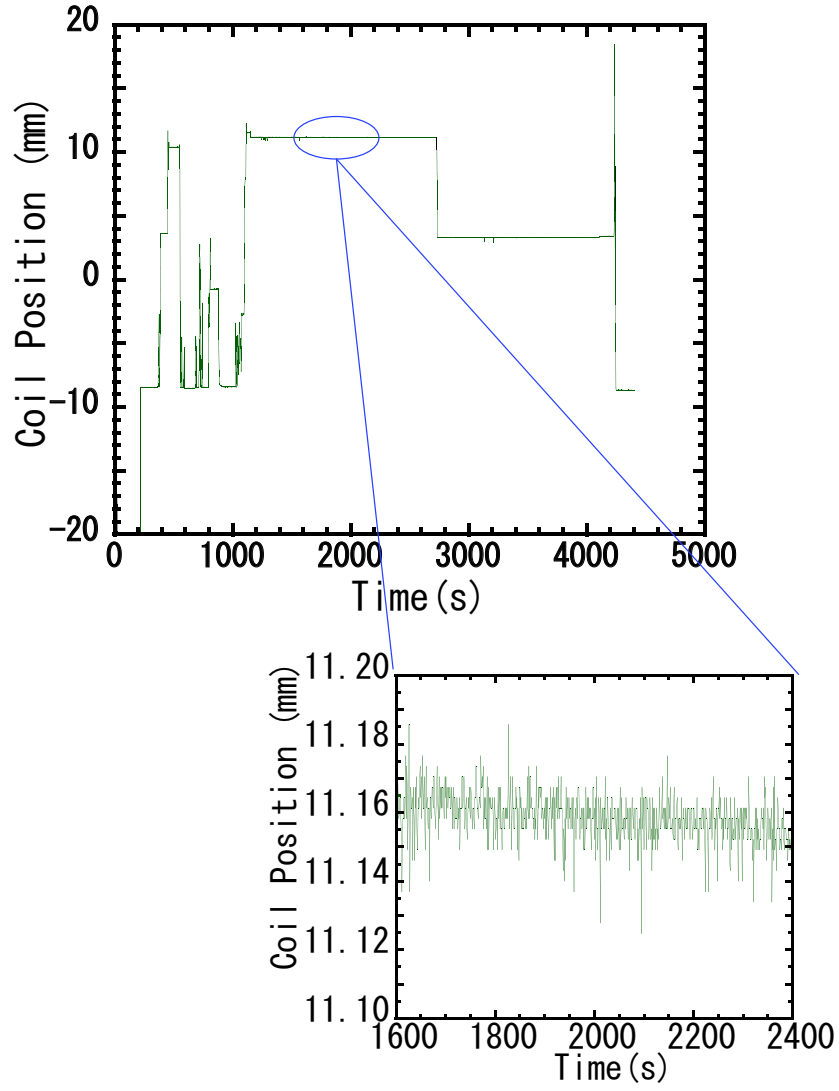


Figure 2.6: Displacement of the internal coil in the test operation. The internal coil was under the stable control for about 1 hour with the accuracy of less than $10\mu\text{m}$. The coil position was changed around 2800 Sec.

Chapter 3

Experimental Setup

So as to investigate the characteristics of plasma, accurate measurements of the plasma density and temperature are indispensable. In this experiments, two type of electrostatic probes (double probe and triple probe) and a 75GHz microwave interferometer have been used for the measurement. In this chapter the principles of these measurement tools are reviewed. Setups of these measurement tools and plasma production system are also described.

3.1 Electrostatic Probe

Although there are numerous measurement methods, electrostatic probes have been widely used for measuring electron density and temperature due to its easiness in the measurement. The measurement method of electrostatic probes is quite simple. A conductor which endures high heat load (e.g., tungsten(W), molybdenum(Mo), tantalum(Ta)) is inserted in plasma and applied voltage. Then a fraction of plasma particle flows into the conductor according to the applied voltage and can be measured as a current. The density and temperature of the electron can be estimated from this voltage-current characteristics. There are three kinds of elec-

trostatic probes: single probe, double probe, and triple probe. Single probes cannot be applied for the plasma produced without electrode because they need reference potential. So in this experiments double and triple probes have been used.

3.1.1 Double Probe

Double probe is a kind of electrostatic probe which uses two probes simultaneously. In double probe measurement, adjacent two conductors, which have the same shape and the same surface area, are inserted into the plasma and voltage is applied between the two conductors. Figure 3.1 shows the typical voltage-current characteristics of the double probe.

The electron temperature T_e can be estimated from the voltage V_c at which the characteristic curve bends,

$$T_e[\text{eV}] = \frac{V_c}{2} . \quad (3.1)$$

The electron density n_e can be calculated from the saturated current I_{is} and the electron temperature estimated by Eq.(3.1) as

$$I_{is}[\text{A}] = 0.61 e^{\frac{3}{2}} n_e [\text{m}^{-3}] \sqrt{\frac{T_e[\text{eV}]}{m_i}} S , \quad (3.2)$$

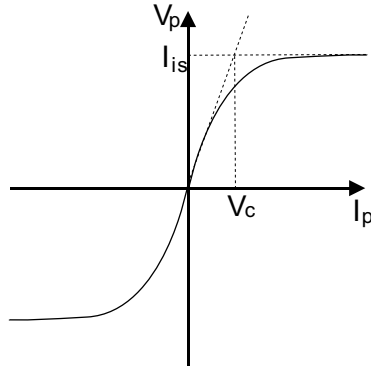


Figure 3.1: Typical current-voltage characteristics measured with a double probe.

where m_i is the ion mass, S is the surface area of conductor. These evaluation method is based on the sheath theory and will be briefly described in Appendix A.

Figure 3.2 shows the drawing of the double probe used in this experiments. In this experiments tungsten rod (cylindrical shape of 0.4mm diameter) was selected for the conductor. The tungsten rod is covered with ceramic tubule for insulation except for 4mm length of the tip which is inserted in plasma. Two covered tungsten rods is inserted in the two-hole ceramic tube and fixed by epoxy adhesive. Figure 3.3 shows the schematic drawing of the double probe circuit. Voltage is swept between -120V and 120V by a bipolar power supply. The applied voltage and the current are measured by digital oscilloscope as a voltage signal along the DC resistor. In measuring the current, the voltage signal generated along the resistor is proportional to the resistance value. So to use a resistor which has higher resistance enables higher S/N ratio. However, a resistor has too high resistance can easily be overheated because the heat generated in the resistor is also proportional to the resistance value. So two circuits of two-series resistor of $1k\Omega$ which are connected in parallel has been used.

If the shape of the conductor is not plane, the current does not saturate when the applied voltage is high enough compared with $\frac{kT_e}{2}$. This is because the effective surface area of the conductor increases due to the increase of sheath thickness when the applied voltage increases. Thus the information of the sheath thickness according to the applied voltage is needed for the accurate estimation of ion saturation current. As described in Ref. 8 and Appendix A, there are the theory of the space charge limited current of cylindrical sheath. However, the estimation of sheath thickness is quite difficult because additional information of the space potential and probe potential are needed. So in this study the ion saturation current is estimated by extrapolating the characteristic curve to the point of zero applied voltage as shown in 3.4. This method can cause the under estimation of the electron density.

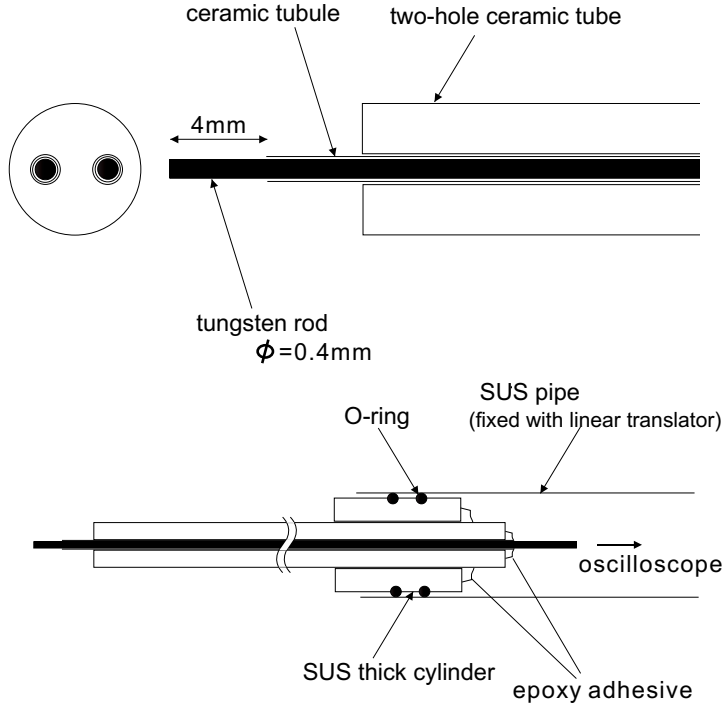


Figure 3.2: Drawing of the double probe used in the experiments

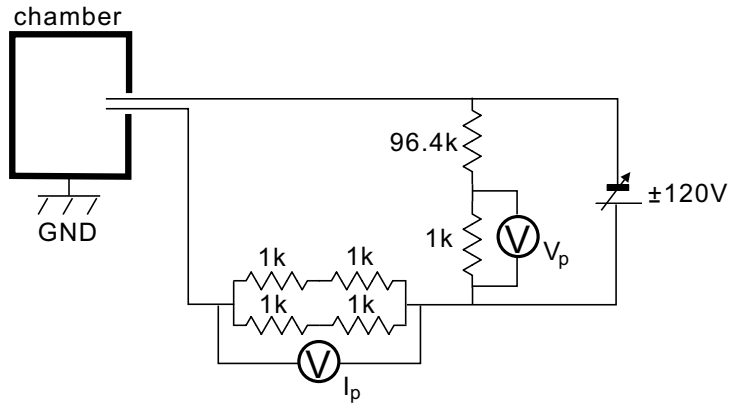


Figure 3.3: Schematic drawing of circuit diagram used in double probe measurement.

The probe current I_p is measured as a voltage signal.

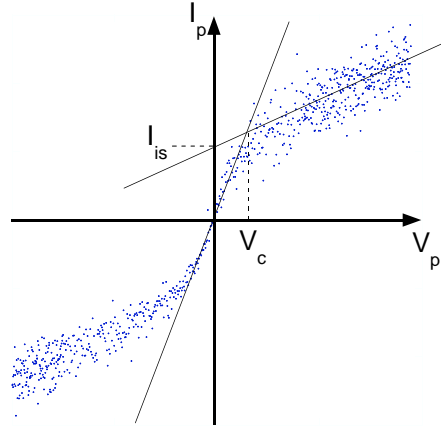


Figure 3.4: Method for estimation of the ion saturation current in the experiments.

3.1.2 Triple Probe

Triple probe uses adjacent three probes simultaneously and applied constant voltage among them. The electron density and temperature are estimated from the instantaneous value of the probe current and voltage. So triple probe does not need the voltage sweeping and enables the measurement with high time resolution.

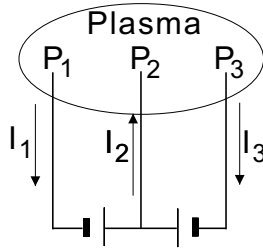


Figure 3.5: Schematic circuit diagram of a triple probe.

There are two major methods in triple probe measurement. The one is called for current method, the other is called for voltage method. In the former method, voltage is applied between one probe and other two probes, as shown in Fig.3.5.

The currents flowing into each probe are given by

$$-I_1 = -I_{e0}e^{\phi_1} + I_i(V_1) \quad (3.3)$$

$$I_2 = -I_{e0}e^{\phi_2} + I_i(V_2) \quad (3.4)$$

$$I_3 = -I_{e0}e^{\phi_3} + I_i(V_3) \quad (3.5)$$

where subscript denotes the probe numbered in Fig.3.5 and $\phi_i = \frac{V_i}{T_e[\text{eV}]}$ ($i = 1, 2, 3$). Assuming the change in ion current by the difference of probe potential is small enough, following relation is satisfied between electron temperature and probe potential.

$$\frac{I_1 + I_2}{I_1 + I_3} = \frac{1 - e^{\phi_2 - \phi_1}}{1 - e^{\phi_3 - \phi_1}}. \quad (3.6)$$

The electron temperature T_e can be estimated from this relation. While ion current I_i is given by

$$I_i = \frac{I_3 - I_2 e^{\phi_3 - \phi_2}}{1 - e^{\phi_3 - \phi_2}}. \quad (3.7)$$

The electron density n_e can be calculated by the same equation as double probe (Eq.(3.2)) with this ion current I_i as

$$n_e[\text{m}^{-3}] = 1.05 \times 10^{15} \frac{I_i}{S} \sqrt{\frac{m_i}{T_e}} \frac{1}{1 - e^{\phi_3 - \phi_2}}. \quad (3.8)$$

In the latter method, the voltage applied between probe 1 and 2 is removed. Then no current flows into probe 2 ($I_2 = 0$) and probe 2 becomes to be floating ($V_2 = V_f$). In this condition, Eqs.(3.6) and (3.7) are reduced into the form

$$\frac{1}{2} = \frac{1 - e^{\phi_f - \phi_1}}{1 - e^{\phi_3 - \phi_1}} \quad (3.9)$$

$$I_i = \frac{I_3}{1 - e^{\phi_3 - \phi_f}}. \quad (3.10)$$

Since in this method high impedance voltage indicator is needed for measuring voltage between probe 1 and 2 to avoid the current flowing into the probe 2, difficulty lies in the measurement of rapid phenomenon due to the inductive noise. However,

this method has advantage that electron temperature T_e can be read directly from the instantaneous value of the probe potential ϕ_1 because potential difference $\phi_3 - \phi_1$ in Eq.(3.9) corresponds to the applied constant voltage, which is known. So in the experiments this method (voltage method) has been adopted for triple probe measurement.

The shape of the used triple probe is similar to the double probe shown in Fig.3.2, except for the number of the tungsten rod is 4. The fourth probe is dummy one for keeping symmetric property. Figure 3.6 shows the schematic drawing of the triple probe circuit. Bias voltage of about 90V is applied between two probes by electric cell connected in series. The two floating potential V_{f1} , V_{f2} , the probe potential V_p , and the probe current I_p are measured as a voltage signal by a digital oscilloscope. Bias voltage V_b is also measured for confirmation.

It is known the influence of change in effective surface area due to the increase of sheath thickness is much smaller in a triple probe measurement than a double probe one.

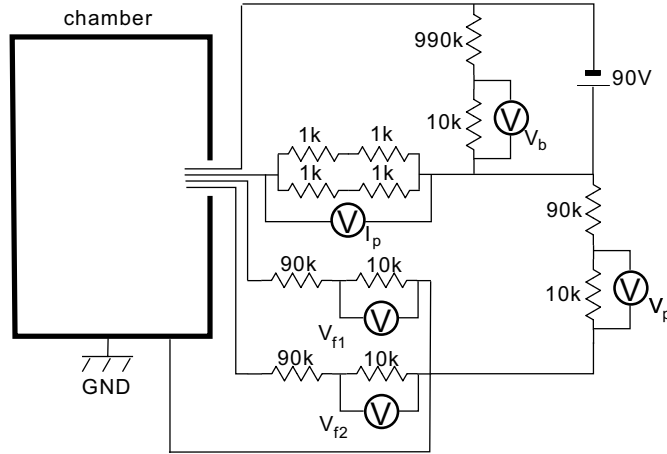


Figure 3.6: Schematic drawing of circuit diagram used in triple probe measurement.

The probe current I_p is measured as a voltage signal.

3.2 Microwave Interferometer

Although electrostatic probes are quite useful, they inevitably disturb the plasma because they need to be inserted directly into the plasma. In addition, there are some difficulties in the analysis of the measured data because the probe measurement is based on several assumptions. So difficulty lies in assuring the reliability of the measured data by the measuring with electrostatic probe only. Thus microwave interferometer, one of a contact-free measurement tool for estimating electron density, has been introduced in this experiments. In proceeding sections, the principle and the setup of these measurement tools are reviewed.

Interferometers are one of an active measurement method which utilize interferometric properties of electromagnetic waves. It is known the refractive index of plasma N depends on the electron density. Then the line-integrated electron density can be estimated from the phase difference $\Delta\phi$ between the signal wave which passes through the plasma and the reference wave which does not. The advantage of this measurement is that the capability of the estimation of the electron density with high time resolution and much smaller disturbance than passive measurement method such as electrostatic probes. However, measured density is line-integrated one and analysis including the estimation of plasma length is needed to obtain the averaged density and density profile.

The principle of interferometry is following. If the frequency of the incident wave ω is high enough and the associated motion of the ions can be negligible, the refractive index of plasma N is given as

$$N^2 = 1 - \frac{2\omega_{pe}^2(\omega^2 - \omega_{pe}^2)/\omega^2}{2(\omega^2 - \omega_{pe}^2) - \Omega_e^2 \sin^2 \theta \pm \Omega_e \Delta} \quad (3.11)$$

$$\Delta^2 = \Omega_e^2 \sin^4 \theta + \frac{4(\omega^2 - \omega_{pe}^2) \cos^2 \theta}{\omega^2} \quad (3.12)$$

where $\omega_{pe} = \frac{e^2 n_e}{\varepsilon_0 m_e}$ is electron plasma frequency, $\Omega_e = \frac{eB}{m_e}$ is electron cyclotron

frequency, and θ is the angle between the direction of the wave propagation and direction of the line of magnetic force $\left(\cos \theta = \frac{\mathbf{k} \cdot \mathbf{B}}{kB}\right)$ (see also Ref. 10) . When the condition

$$\Omega_e^2 \sin^4 \theta \gg \frac{4(\omega^2 - \omega_{pe}^2) \cos^2 \theta}{\omega^2} \quad (3.13)$$

is satisfied, there exist two mode of waves of which refractive index are

$$N^2 = \frac{\omega^2 - \omega_{pe}^2}{\omega^2 - \omega_{pe}^2 \cos^2 \theta} \quad (3.14)$$

$$N^2 = \frac{(\omega^2 - \omega_{pe}^2)^2 - \omega^2 \Omega_e^2 \sin^2 \theta}{\omega^2(\omega^2 - \omega_{pe}^2) - \omega^2 \omega_{pe}^2 \sin^2 \theta} . \quad (3.15)$$

Interferometry utilizes the property of the wave of Eq.(3.14). If the wave propagates perpendicular direction against the line of magnetic force $\left(\theta = \frac{\pi}{2}\right)$, Eq.(3.14) is reduced to the form

$$N = \sqrt{1 - \frac{\omega_{pe}^2}{\omega^2}} . \quad (3.16)$$

If $\omega \gg \omega_{pe}$ is satisfied, N can be approximated as

$$N \simeq 1 - \frac{\omega_{pe}^2}{2\omega^2} \quad (3.17)$$

While the phase variance $\Delta\phi$ of the wave which propagates the plasma of length d is given by

$$\Delta\phi = \int_0^d (k_v - k_p) dx = k_v \int_0^d (1 - N) dx \quad (3.18)$$

where k_v and k_p is wave number of the wave in vacuum and plasma, respectively. Then using the relation of $\omega = k_v c$ and $c = f\lambda$, the fringe shift of the wave is written in the form

$$\frac{\Delta\phi}{2\pi} = \frac{e^2 \lambda \int_0^d n_e dx}{8\pi \epsilon_0 m_e c^2} = 4.485 \times 10^{-16} \lambda \int_0^d n_e dx. \quad (3.19)$$

Since the wavelength of the wave λ is already known, line integral density can be obtained. If the length of measured plasma is known, line average electron density \bar{n}_e can be calculated. It is easily understand from Eq.(3.16) that the refractive

index N becomes zero as the frequency ω becomes close to the electron plasma frequency ω_{pe} . This phenomenon is called for cutoff, and gives the upper limit of the measurable density. The lower limit depends on the measurement system. Generally detectable fringe is 0.01 (corresponds to the phase shift of 3.6 degree) .

Figure 3.7 shows the circuit diagram of the developed interferometer. According to the fact that the measured electron density in the past experiments are the order of 10^{16}m^{-3} , 75GHz microwave, which has wavelength of 4mm and cutoff density of $7 \times 10^{17}\text{m}^{-3}$, was selected for this experiments. The interferometer consists of three part: main unit, transmission system and receive system. The main unit includes oscillators for the signal wave and the reference wave. The phase shift $\Delta\phi$ is detected as the voltage signal proportional to the value of $\cos \Delta\phi$ by mixing the waves of signal and reference path. The measurable lower limit of the density is determined by the value which satisfies enough S/N ratio. At present the lower limit is less than $1 \times 10^{15}\text{m}^{-3}$. The microwave for measurement is transmitted and received by opposed two lens horn antennae attached on the Mini-RT device. The interferometer ideally has a space resolution less than the diameter of the antenna because transmitted microwave is focused by the lens horn antenna. Thus these antennae assumed to be moved horizontally and vertically in the port window. While, the wave must be transmitted by a waveguide in order to reduce attenuation because in this system a 75GHz microwave is used. However, if the main unit and the transmission/receive system are all connected by the rigid waveguide, whole system must be moved with the move of the horn antennae. Thus this system introduced three multipliers of wave frequency, which enable the wave transmission between the main unit and transmission/receive system with low frequency by flexible co-axial cables. So 18.752GHz phase lock oscillator (PLO) was adopted for generating the signal wave in the main unit.

To obtain line-averaged electron density, the information of plasma length d

and the proportional coefficient on $\cos \Delta\phi$ signal are needed. In this experiments, the plasma length is estimated by the position of last closed flux surface (LCFS) obtained through calculation of the magnetic configuration. It also can be estimated by the probe measurement. The proportional coefficient is obtained from measurement of peak output voltage with varying the distance between two horn antennae continuously. At present this peak value is around 200mV. The linear guiding system for moving the horn antenna and will be described in the Sec.3.4.

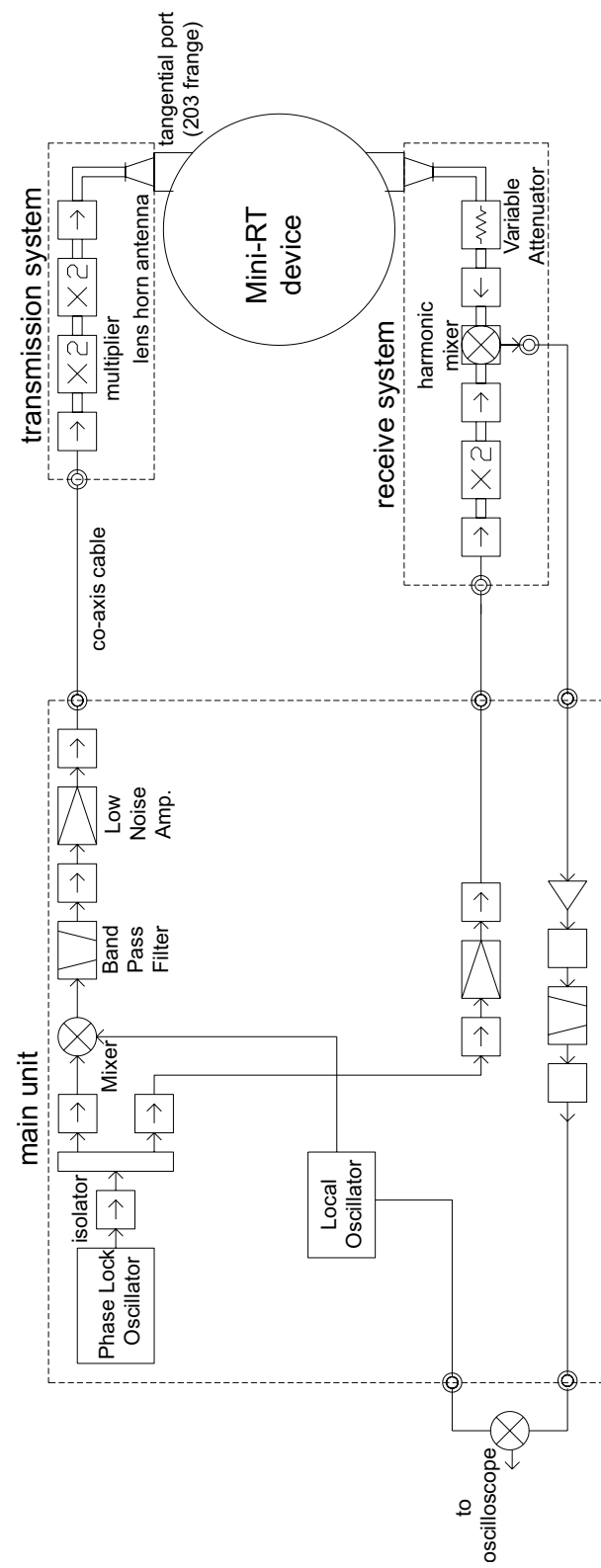


Figure 3.7: Schematic circuit diagram of the microwave interferometer

3.3 Plasma Production System

The Mini-RT device uses a 2.45GHz microwave for plasma production. Plasma is produced by electron cyclotron resonance heating (ECH) at the 875G magnetic surface. The physics of ECH will be described later in Sec.5.1. In this section, the brief view of the microwave launching system is given.

Fig 3.8 shows a photograph of the waveguide for a 2.45GHz microwave (wavelength of about 12cm). The microwave is generated by a gyrotron, shown in the right side of the figure. The generated wave power is up to 3kW. The wave is horizontally transmitted thorough insulated waveguide and square waveguide. The vertically long component is the E-H tuner for the impedance matching. This E-H tuner can be remotely controlled by two stepping motors. After passing the E-H tuner, the wave is bend and launched obliquely into the vacuum vessel. The waveguide is inclined at 30 degree to the upright. The relatively wide components located immediately after the bend is the twist waveguide which rotates the polarization plane by 90 degree. To replace this twist waveguide of normal square waveguide, the polarization of incident wave can be changed. To use square waveguide, the direction of electric field of the incident wave is parallel to the magnetic field (O-mode). To use twist waveguide, the direction of electric field is perpendicular to the magnetic field (X-mode).

3.4 Setup of the Measurement Tools

The Mini-RT device has total 27 ports in four different size (horizontal:ICF304 \times 3, ICF203 \times 4, vertical:ICF152 \times 2, ICF70 \times 16, oblique:ICF152 \times 2) . In this experiments 4 horizontal ports have been used for measurement and 1 oblique port has been used for microwave injection.

Measurement system use horizontal ports located on the side surface of the vac-

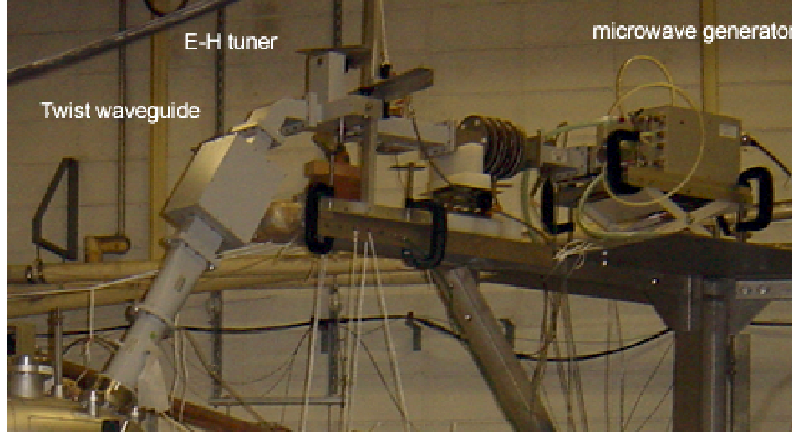


Figure 3.8: Photograph of the 2.45GHz ECH system.

uum vessel. Figure 3.9 shows the location of the measurement system. The west horizontal port is used for triple probe. The probe fixed with the linear translator attached on this port, and can move along radial direction between $R=0.21\text{m}$ (corresponding to the outer surface of internal coil) and 0.40m . The south-west horizontal port is used for double probe. On the port also the linear translator is attached and the probe can move between $R=0.21\text{m}$ and 0.50m (corresponding to the vacuum vessel wall) . The microwave interferometer uses two opposite horizontal ports (which called for tangential port) . These ports have a quartz window and one can see plasma along the tangential line. Basically the lens horn antennae fixed at the center of the port, which corresponds to radius $R = 0.281\text{m}$ on the equatorial plane. Figure 3.10 is a photograph of the horn antenna attached on the tangential port. The horn antenna is fixed on the linear guide stage. Figure 3.11 shows the movable region of the horn antenna in the port. Both antennae can move along the horizontal direction with the range of $\pm 40\text{mm}$ and the vertical direction with the range of 30mm from the basic position by linear guide. When the antenna moves to the vertical direction, the movable range of horizontal direction slightly decreases

due to the circular shape of the window. The transmission antenna can also move back and forth by the micrometer screw with the accuracy of $50\mu\text{m}$. This is used for the phase adjustment and the measurement of peak output voltage. The 4 mm motion in this direction corresponds to the 2π phase shift.

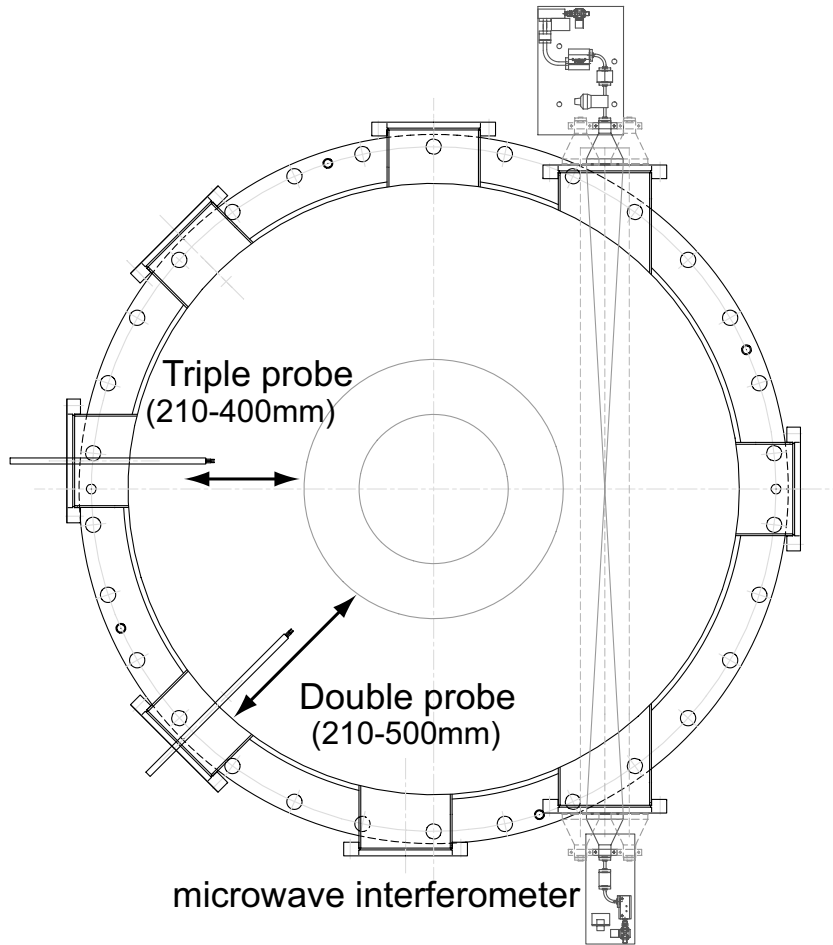


Figure 3.9: Location of the measurement system. The double/triple probe is fixed with the linear translator and can be moved in radial direction. The microwave interferometer is attached on opposite tangential ports. See also Fig.3.11.

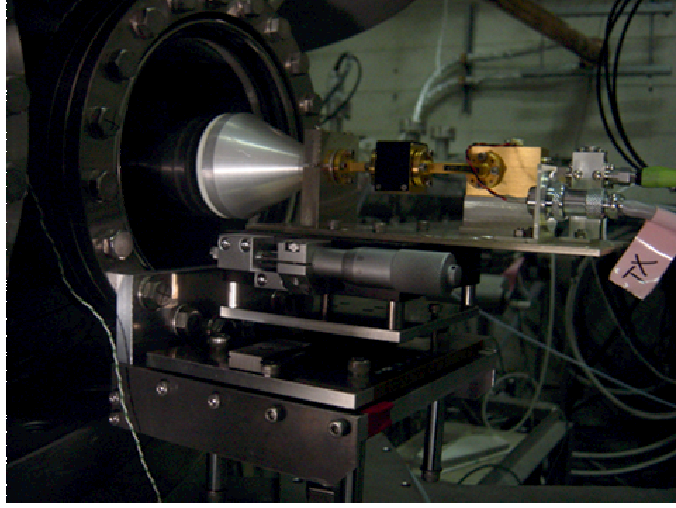


Figure 3.10: Photograph of the lens horn antenna fixed on the linear guide stage attached on the tangential port.

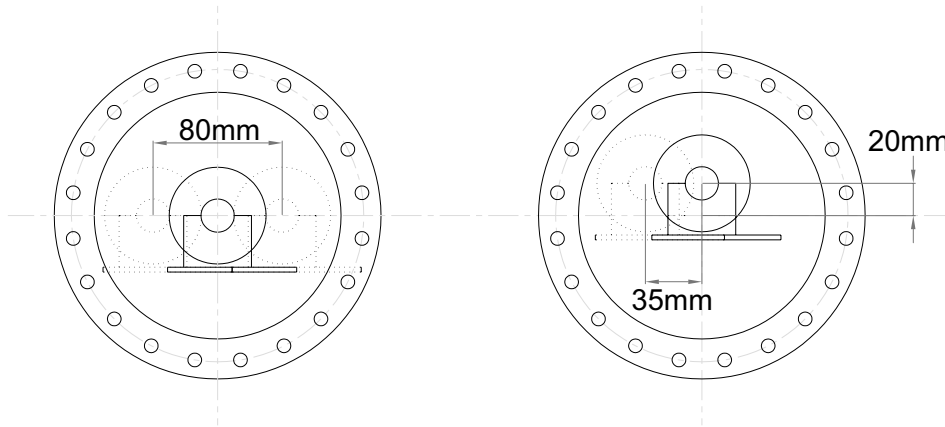


Figure 3.11: Setup of the lens horn antenna of the microwave interferometer. The left/right figure shows the movable range of the horizontal direction when the antenna locates in the vertical position of 0mm and 20mm. Other components of the interferometer and linear guide stage are not shown.

Chapter 4

Experimental Results

One of the main objective of this study is to clarify the effect of the removal of the supporting structure by the levitation of the internal coil. So experiments with the supported and levitated internal coil have been carried out in order to investigate the difference in plasma properties whether the internal coil is supported or levitated. In this chapter the results from these experiments are described.

4.1 Experiments with Supported Internal Coil

In this section, the results from the plasma experiments with the supported internal coil is reviewed. In this experiments, electron density and temperature under various condition of the injected microwave power and the neutral gas pressure have been measured so as to comprehend the plasma property with the supported internal coil. All experiments used H_2 gas for plasma production.

Figure 4.1 shows a photograph of the plasma with the supported internal coil. It can be seen the plasma exists whole region in the vacuum vessel. It also can be recognized the dipole magnetic field configuration. The calculated magnetic configuration of this condition is shown in Fig.4.2. The magnetic surfaces are concentric

and basically closed except for the interruption by the internal coil and supporting structure. The measured region of probes and interferometer also shown in Fig.4.2.

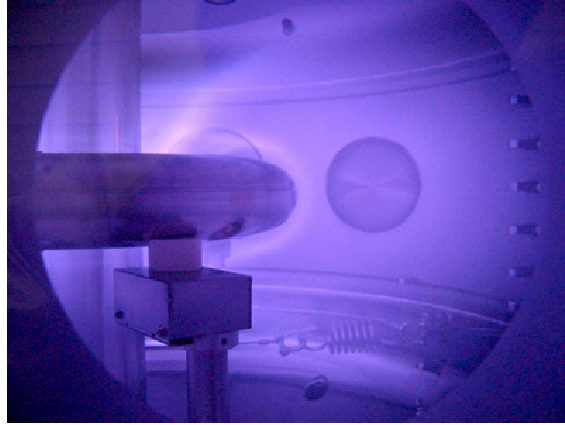


Figure 4.1: Photograph of the plasma with supported internal coil.

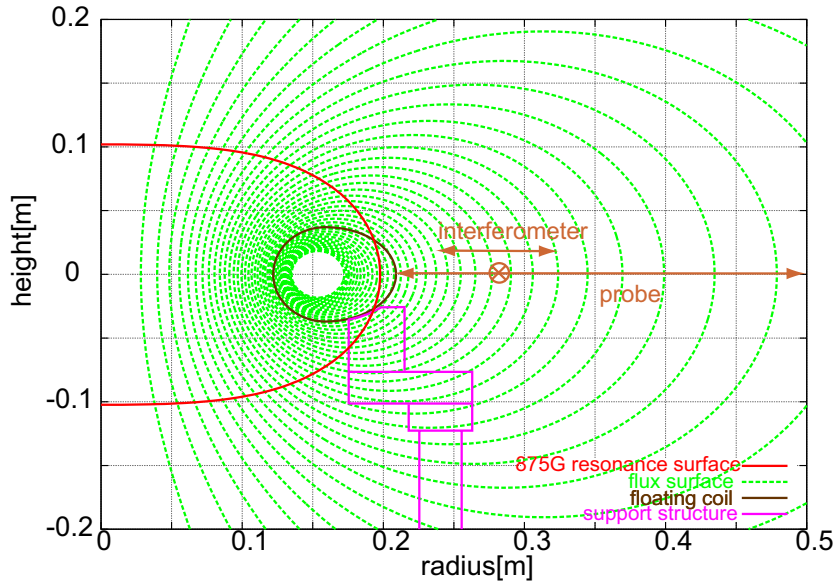


Figure 4.2: Magnetic configuration and the location of the internal coil and support structure when the internal coil is supported.

Figure 4.3 and 4.4 show the typical profiles of electron density and temperature, respectively. These data was measured by double probe. In this measurement, the neutral gas pressure was 4.0×10^{-2} Pa, with which the stable plasma production had been possible in past experiments, and injected ECH power was 2.5kW. It can be seen the electron density sharply rises from the surface of the internal coil, $R = 0.21$ m, and has a peak around $R = 0.26$ m, about 50mm from the surface of the internal coil. Then the electron density decreases gradually to the out wall of the vacuum vessel (correspond to $R = 0.50$ m). The peak density is about $7 \times 10^{16}\text{m}^{-3}$. Although the peak value changes by the injected microwave power, basically the electron density of the plasma with the supported internal coil is the order of 10^{16}m^{-3} . The neutral gas density calculated from the pressure is $8 \times 10^{18}\text{m}^{-3}$. Thus the ionization degree is less than 1%. While the electron temperature profile is relatively flat and the measured value is around 5–6eV in whole region.

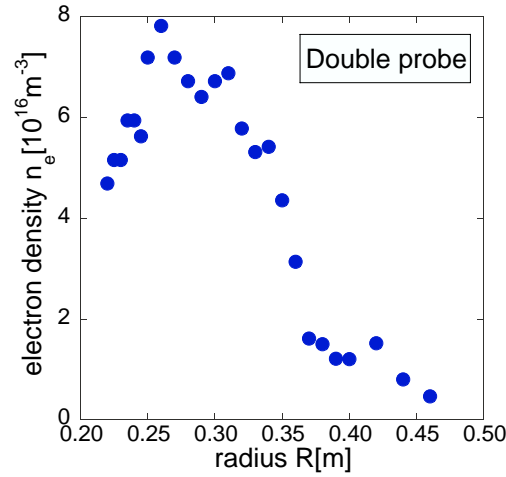


Figure 4.3: Electron density profile with supported internal coil measured by double probe.

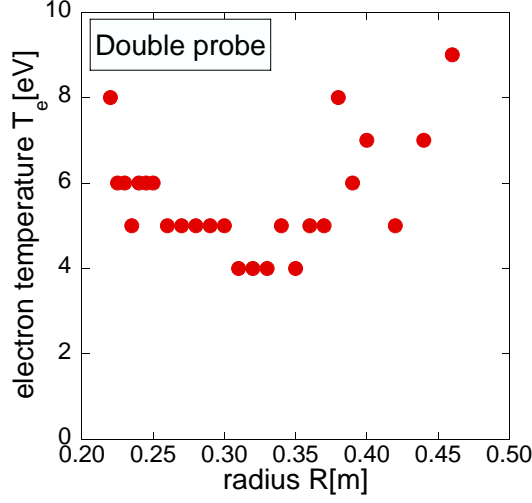


Figure 4.4: Electron temperature profile with supported internal coil measured by double probe.

To make sure of this double probe measurement, cross-check with the interferometer was carried out. For simplicity, the cross-check was done by means of comparing the line-averaged electron density measured by the microwave interferometer with the calculated one obtained from the electron density profile measured by the double probe. Figure 4.5 shows this result. The closed circle represents the line-averaged electron density obtained from the microwave interferometer measurement with using Eq.(3.19). While the open circle represents the calculated value from the profile data measured by the double probe (already shown in Fig.4.3). Where the plasma length d is assumed to be the same as the distance between walls along the microwave path (i.e. if the position of lens horn antenna is 0.28m, $d = 2 \times \sqrt{0.5^2 - 0.28^2}$, see Fig.4.6) .

Strictly line-averaged density must be calculated as

$$\bar{n}_e = \frac{1}{d} \int_0^d n_e(x) dx , \quad (4.1)$$

but the measured profile is discrete one. One method of this calculation is using

fitting curve of this discrete profile. However, this case needs only rough estimation.

So the calculation was carried out just as follows:

$$\bar{n}_e = 2 \times \frac{\sum_{i=0}^k \left\{ \frac{n_e(\theta_i) - n_e(\theta_{i-1})}{2} \right\} \{r_{i-1} \cos(\theta_{i-1}) - r_i \cos(\theta_i)\}}{\sum_{i=1}^k \{r_{i-1} \cos(\theta_{i-1}) - r_i \cos(\theta_i)\}} \quad (4.2)$$

where r_i ($i = 1, 2, \dots$) represents discrete radial position at which double probe measured density, $\theta_i = \arcsin \frac{r_i}{L}$, θ_0 and θ_n are $\arcsin \frac{0.5}{L}$, $\frac{\pi}{2}$, respectively (see Fig.4.6). The estimated value is good agreement with the measured value within 10% deviance. This result indicates that the accuracy of the probe measurement is assured.

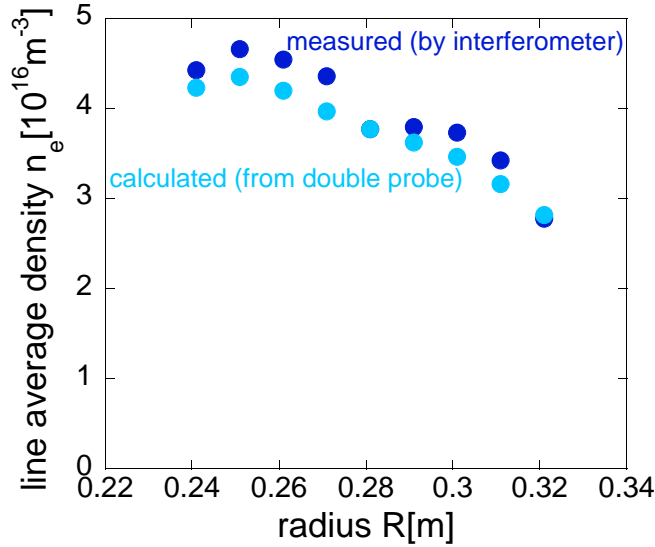


Figure 4.5: Comparison of line-averaged electron density. Closed circle represents measured data by the interferometer. Open circles represents calculated data obtained from density profile measured by double probe (shown in Fig.4.3)

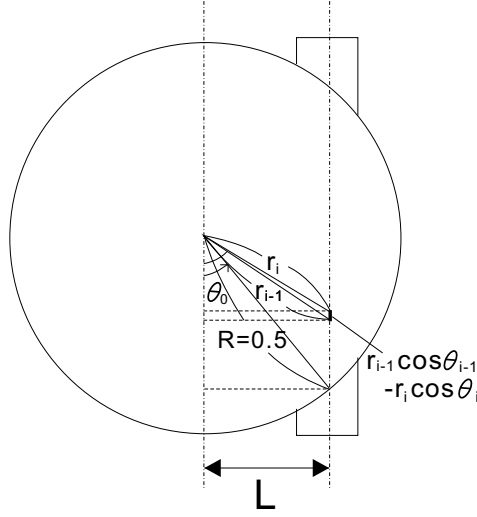


Figure 4.6: Calculation method of line-averaged density from discrete radial data.

Figure 4.7 and 4.8 show the ECH power dependence of electron density and temperature, respectively. This measurement was carried out by double probe fixed at the point of radius $R = 0.24\text{m}$ and the neutral gas pressure is the same value as the previous experiments: $4 \times 10^{-2}\text{Pa}$. The same data measured by triple probe is shown in Fig.4.9 and 4.10. These figures show that electron density increases as the injected ECH power is increasing. While electron temperature is not sensitive on the ECH power. Both (double and triple probe) data may indicate that the density is not proportional to the ECH power and has the jump around the ECH power of 2kW. At present the reason of this jump is not clear. One assumption is that it is caused by the change in the density profile. Since the position of $R = 0.24\text{m}$ is near the peak, a slight variation in the profile cause a significant change of the density around the peak. So total density is thought to be proportional to the ECH power. Actually, line-averaged density is almost proportional to the ECH power, as shown in Fig.4.11.

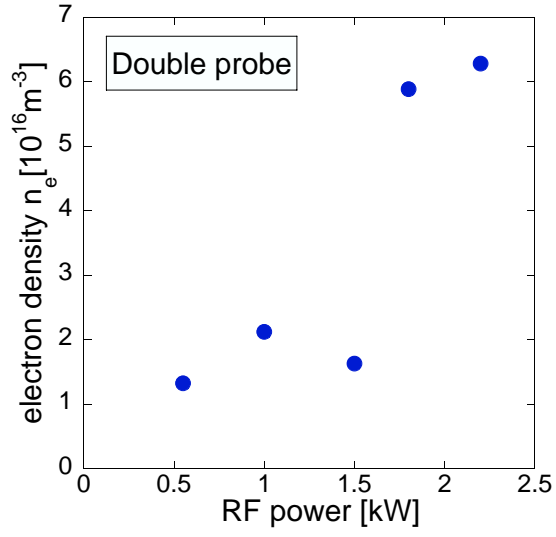


Figure 4.7: ECH power dependence of electron density with supported internal coil measured by double probe. Probe position is $R=0.24\text{m}$.

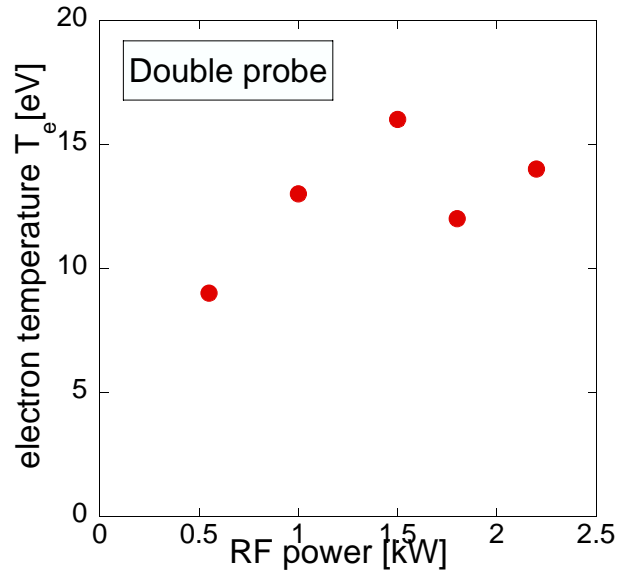


Figure 4.8: ECH power dependence of electron temperature with supported internal coil measured by double probe. Probe position is $R=0.24\text{m}$.

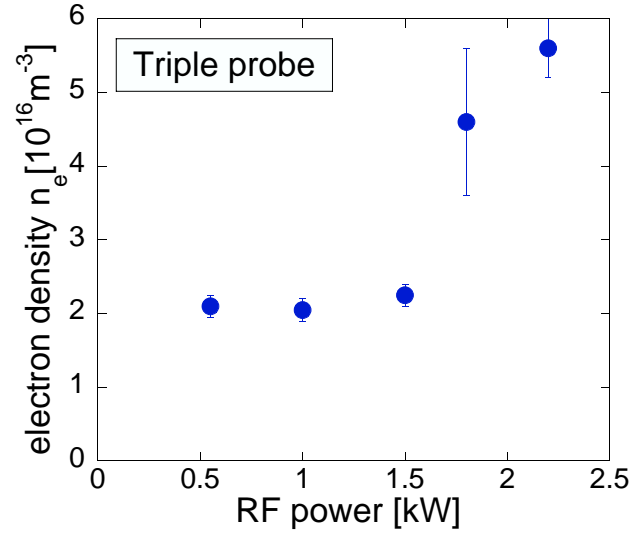


Figure 4.9: ECH power dependence of electron density with supported internal coil measured by triple probe. Probe position is $R=0.24\text{m}$.

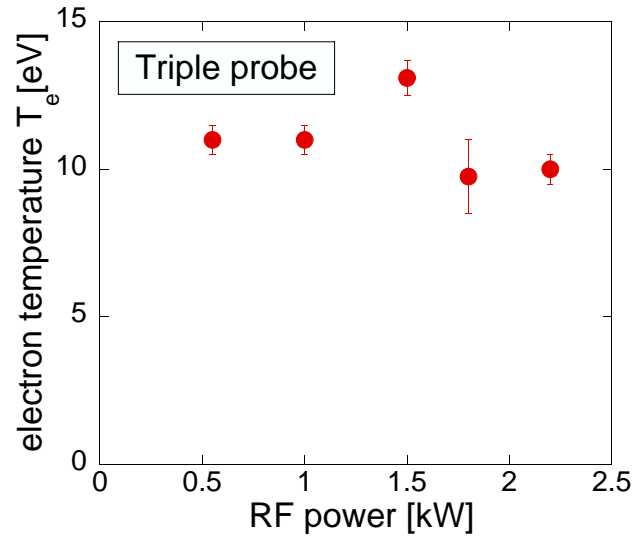


Figure 4.10: ECH power dependence of electron temperature with supported internal coil measured by triple probe. Probe position is $R=0.24\text{m}$.

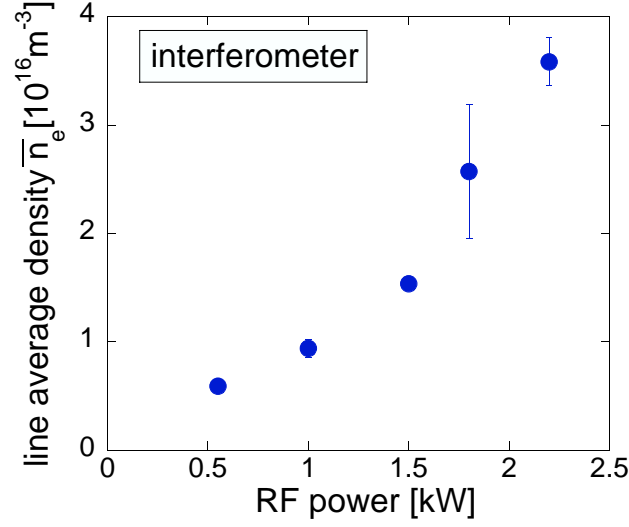


Figure 4.11: ECH power dependence of line-averaged electron density with supported internal coil measured by microwave interferometer. The position of interferometer corresponds radius of 0.28m.

The knowledge obtained from these measurements is following:

- Although electron density is proportional to the injected ECH power, it reaches $7 \times 10^{16} \text{m}^{-3}$ at most.
- Electron temperature is relatively low ($\lesssim 10 \text{eV}$), regardless of the injected ECH power.

It is assumed the electron density is limited by the cut off density, where $7.4 \times 10^{16} \text{m}^{-3}$ for the 2.45GHz wave. Since the ionization degree is less than 1%, the plasma is assumed to be in the regime in which collision of electrons with neutral gas molecules is dominant. The collision time of electron with neutral molecule τ_{en} is calculated by

$$\tau_{en} = \frac{1}{n_n \sigma_{en} v_{\text{th},e}} \quad (4.3)$$

where n_n is the neutral gas density, σ_{en} is the collisional cross-section of the electron

with the neutral gas, and $v_{th,e} = \sqrt{\frac{kT_e}{m_e}}$ is thermal velocity of the electron. In fact, the calculated collision time is 1.0×10^{-6} sec, which is shorter than electron-ion or electron-electron collision time ($\sim 5 \times 10^{-6}$ sec) and electron-electron temperature relaxation time ($\sim 10^{-5}$ sec) . This assumed to be the reason why the electron temperature does not increase so much. In order to get out of this regime, the increase of ionization degree by decreasing the neutral gas pressure is indispensable. Plasma production under the condition of neutral gas pressure of less than 4.0×10^{-4} Pa enables full ionization with the electron density same as obtained in the experiment with the supported internal coil. However, in the experiments the electron density immediately fell off as neutral pressure was decreasing, and under the condition of neutral pressure of less than 1×10^{-2} Pa, plasma production became impossible. Then one assumption arises that the collision with the support structure in the plasma causes the energy loss of the electrons and prevent the increase of the electron temperature. Thus the same experiments with the condition that the internal coil is levitated and support structure is totally removed from plasma region is necessary.

4.2 Experiments with Levitated Internal Coil

In this section, the results from the plasma experiments with the levitated internal coil is presented. In this experiments, the measurements of electron density and temperature with the condition that the internal coil is levitated have been carried out, and the effect of the removal of supporting structure by the levitation of the internal coil on the plasma parameters have been investigated through the comparison the results with the one obtained in the experiment with the supported internal coil. In this experiments, the internal coil was levitated about 25mm from the equatorial plane and the support structure was descended 20mm. Figure 4.12

shows the calculated magnetic configuration and the position of the internal coil, the support structure, and the measurement tools in this condition. Figure 4.13 shows a photograph of the plasma with the levitated internal coil. It can be seen that plasma exists only in the region enclosed by the separatrix that emerges between the internal coil and the levitation coil. In Figure 4.13, the measured ranges of the probes and the interferometer are also shown. Since the probes were fixed on the equatorial plane, the measured data by the probes can be different from the data of the same radius on the height of the internal coil. The interferometer was moved above in accordance with the coil levitation. Though the levitation of the coil was 25mm, the displacement of the interferometer was confined in 20mm so as to keep enough horizontal movable range.

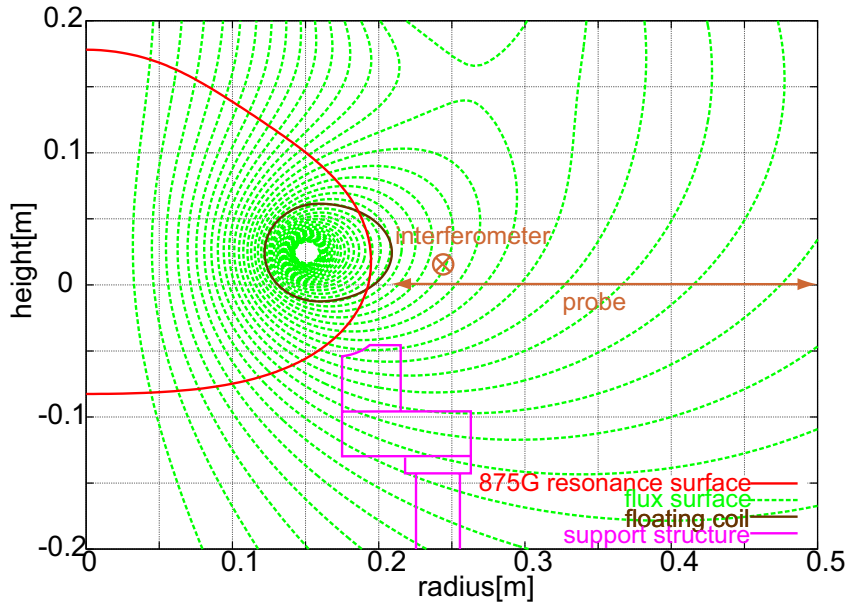


Figure 4.12: Magnetic configuration and the position of the internal coil, support structure, and measurement tools when the internal coil is levitated.

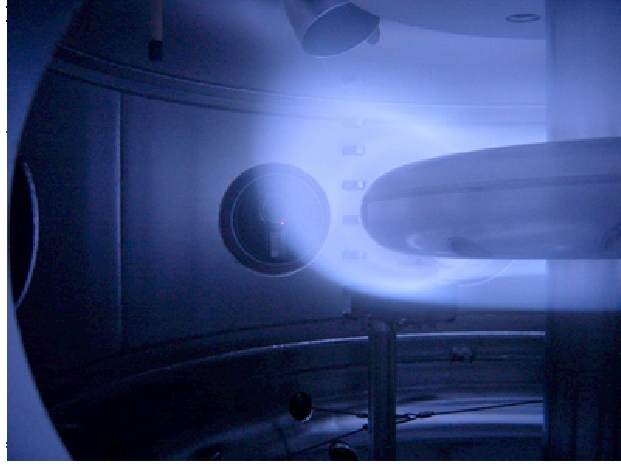


Figure 4.13: Photograph of the plasma with levitated internal coil. It can be shown the separatrix from plasma shape.

Figure 4.14 and 4.15 shows the dependence on neutral gas pressure of electron density and temperature measured by the double probe. In this measurement, the probe position was fixed at $R = 0.24\text{m}$ and injected ECH power was around 2kW . When the internal coil is supported, it can be seen that the electron density drastically decreases as the neutral gas pressure is decreasing, and plasma production with the neutral gas pressure below $1 \times 10^{-2}\text{Pa}$ is impossible. In contrast, when the coil is levitated, such decrease in the density does not occur. In the experiments, plasma production at the neutral gas pressure of $1 \times 10^{-3}\text{Pa}$ was successfully carried out. In addition, it can be seen that the electron density increases as the gap length between the internal coil and the supporting structure is increasing. So relation between the gap length and electron density at the constant neutral gas pressure have also been measured. Figure 4.16 and 4.17 show the results measured by the double probe and the microwave interferometer, respectively. In this measurement, probe position was fixed at $R = 0.24\text{m}$, and interferometer was set at the point corresponds to the radius of 0.25m . The neutral gas pressure was about $3 \times 10^{-3}\text{Pa}$.

It is apparent that the density at the probe position increases as the gap length is increasing. Considering the line-averaged density measured by the interferometer is reflected the density from the vacuum vessel wall to the radius of $R = 0.25\text{m}$, the density assumed to increase in the whole plasma region as well as the region near the probe position. These results coincide with the expectation of the energy loss of the plasma due to the existence of support structure. Rough estimation based on the assumption, which the electron which has enough energy to ionize an H_2 gas molecule is lost by the collision with the support structure, also supports this expectation (see Appendix B). This indicates the levitation of internal coil accompanied with the removal of the support structure may realize the high density, high temperature plasma production.

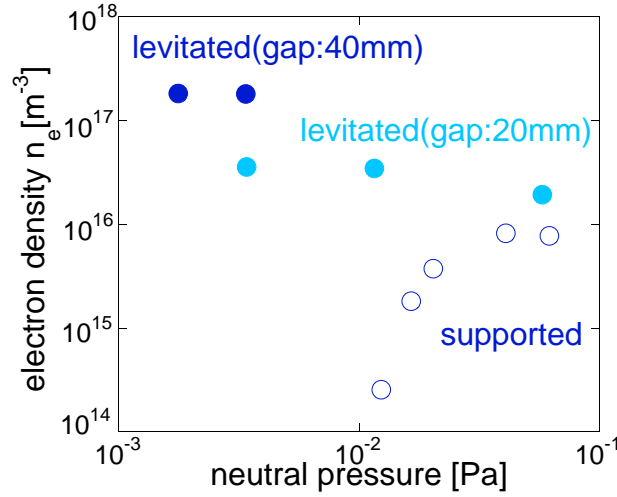


Figure 4.14: Neutral pressure dependence of electron density measured by double probe.

Probe position is $R=0.24\text{m}$.

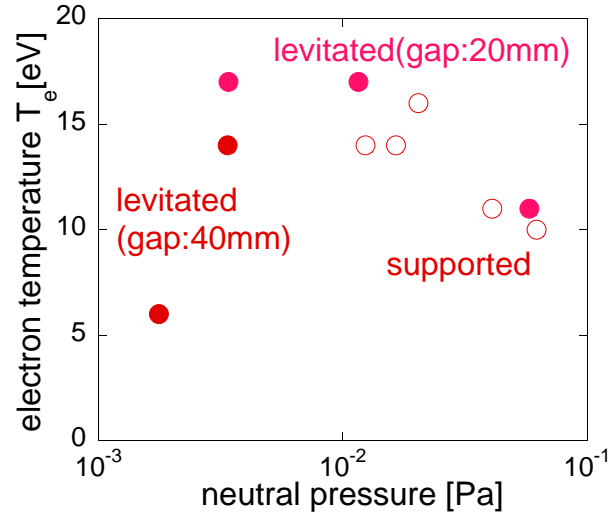


Figure 4.15: Neutral pressure dependence of electron temperature measured by double probe. Probe position is $R=0.24\text{m}$.

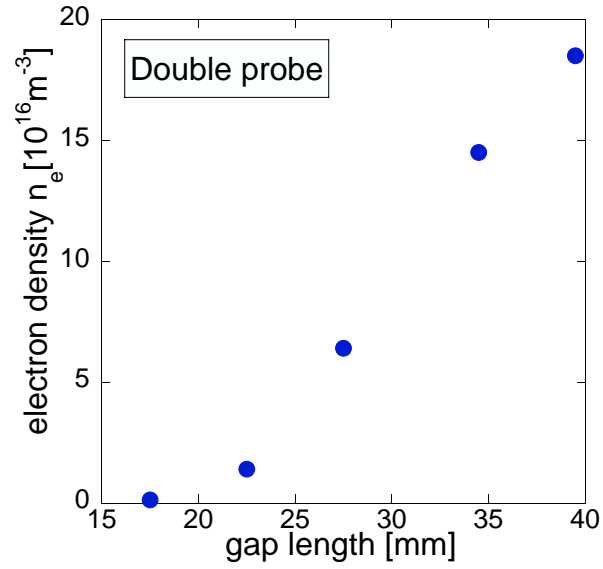


Figure 4.16: Variation of electron density for several gap length between the floating internal coil and the support structure.

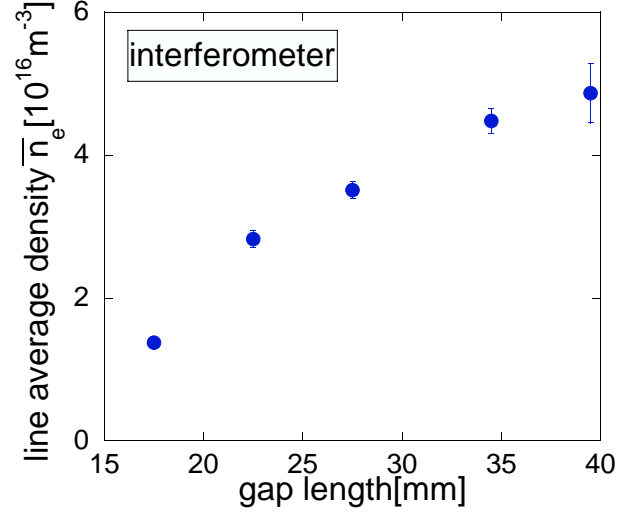


Figure 4.17: Variation of line-averaged electron density for several gap length between floating internal coil and support structure.

Figure 4.18 and 4.19 show the density and temperature profile measured by triple probe when the internal coil is levitated. In this measurement, the neutral gas pressure is $1.5 \times 10^{-3} \text{ Pa}$ and injected ECH power is around 2.5kW. The result obtained by the experiments with supported internal coil is also plotted for comparison. Note the neutral gas pressure is different in both cases. It is apparent that the plasma region shrinks and becomes to be localized around the internal coil when the internal coil is levitated. So the density and temperature gradients are steep compared with the supported case. This is because that the existence of separatrix and magnetic surfaces outer than it are not closed and ended by the vacuum vessel wall. Figure 4.20 shows the calculated shape of the last closed flux surface (LCFS) of this experimental condition. The calculated position of the magnetic surface which passes the separatrix on the equatorial plane is around $R = 0.28 \text{ m}$, which is in good agreement with the position of the density drop. Although this agreement is important, major difference which should be remarked is the absolute value of

them. Although the peak value is unknown in the levitated case, the maximum measured electron density is much higher ($1.6 \times 10^{17} \text{m}^{-3}$), about twice of the peak density of the supported case. It is far beyond the cutoff density of the 2.45GHz microwave ($7.4 \times 10^{16} \text{m}^{-3}$). Unfortunately, the interferometer cannot see the region around such high density due to the limitation of the window size. However, the line-averaged electron density reaches $6 \times 10^{16} \text{m}^{-3}$, which is 1.5 times of the value obtained in the supported case. So it is possible that the overdense plasma is produced. The electron temperature also increase and in most region the value is about twice of the one obtained in the supported case. It can be seen the existence of low temperature region around $R = 0.27\text{m}$. This temperature drop is also seen in double probe data, but the drop is smaller than that of triple probe. At present there is no physics explanation to describe this drop. One assumption is that this drop is the apparent one which was caused by a misinterpretation of the measured data and there were no actual temperature drop. The quite steep density gradient may cause an misinterpretation in the probe measurement. Especially, the four conductor of the triple probe strictly do not locate on the same magnetic surface because the magnetic surface is curving in vertical direction. In the experiments with levitated internal coil, this effects is emphasized because the position in which magnetic surface has small curvature moves above with the internal coil. If densities that is seen by four conductor is different each other, several assumption considered in analysis of probe data cannot be satisfied. In addition, in such steep density gradient can cause a negligible flow or drift driven by pressure gradient. Since the flow direction of the pressure driven drift is perpendicular to the probe, the current flow into the conductor is quite different whether it locates upstream or downstream of the flow. To verify this problem, a cross check by other technique to measure electron temperature is needed.

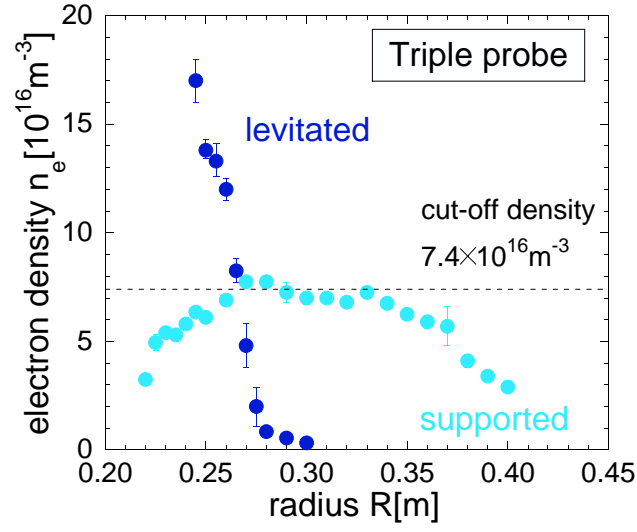


Figure 4.18: Electron density profile with levitated internal coil measured by triple probe. The data with supported internal coil is also shown for comparison.

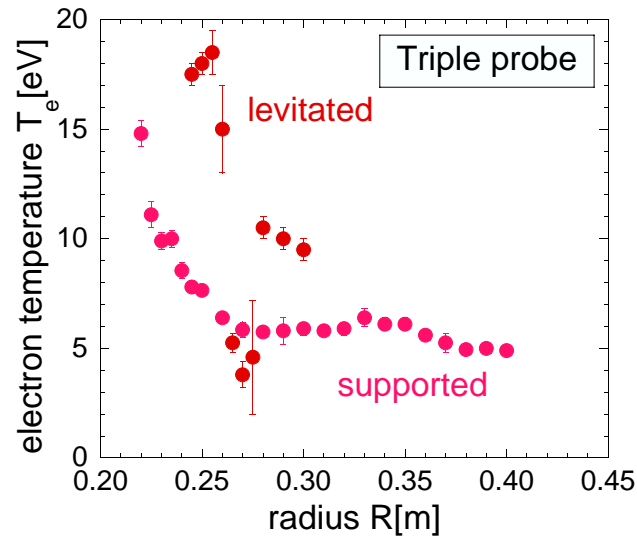


Figure 4.19: Electron temperature profile with levitated internal coil measured by triple probe. The data with supported internal coil is also shown for comparison.

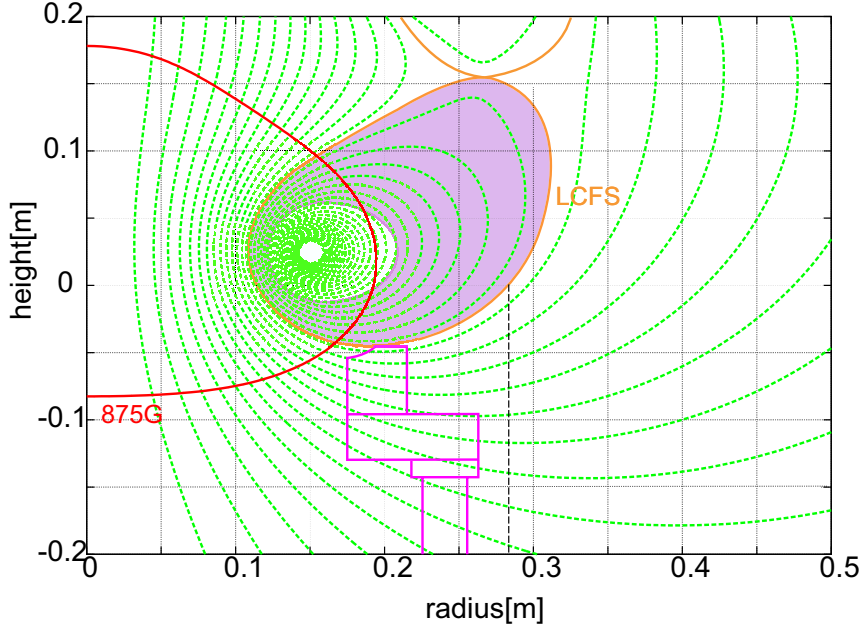


Figure 4.20: The calculated shape of the magnetic configuration and last closed flux surface (LCFS) under the condition of the experiment with the levitated internal coil.

There are another results that indicate the additional effect of the levitation of the internal coil. Figure 4.21 and 4.22 show the waveform of the density decay measured by the interferometer with the supported and levitated internal coil. The time resolution of these measurement were $1\mu\text{sec}$. Since injected ECH power cannot be shut off instantaneously due to the performance of the gyrotron, it is difficult to estimate the plasma confinement time from these data. So here only the comparison of the decay time constant has been carried out. When the internal coil is supported, the decay time constants of ECH power and density are both about 20msec. In contrast, when the internal coil is levitated, the decay time constants of ECH power and density are about 20msec and 45msec, respectively. This difference does not immediately indicates the amount of the confinement time. But it can be said that the improvement of confinement is occurred by the levitation of the internal coil.

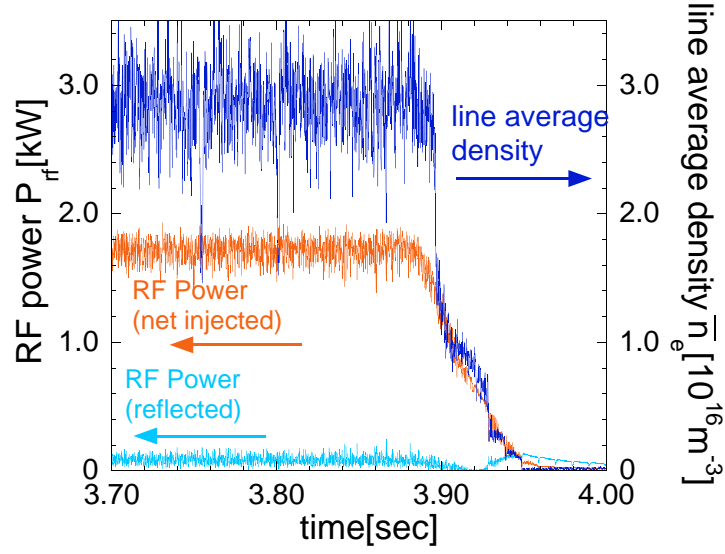


Figure 4.21: Waveforms of the line-averaged electron density and ECH power decay with the condition that the internal coil is supported.

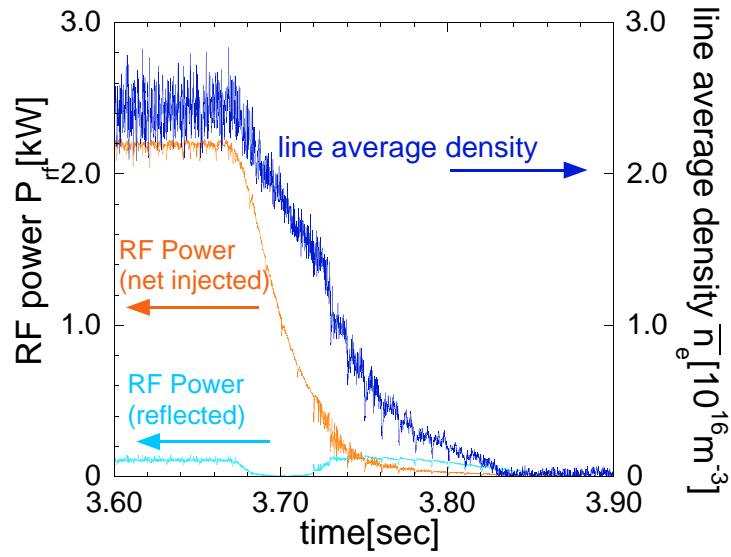


Figure 4.22: Waveforms of the line-averaged electron density and ECH power decay with the condition that the internal coil is levitated.

It becomes clear that the removal of support structure in the plasma by levitating the internal coil causes several improvement of plasma properties: the increase of the density, the increase of ionization degree, the improvement of confinement. However, the beta value calculated from the electron density and temperature at the point of peak density is only 0.06%. So further increase of the electron density and temperature are desired. It is assumed that the still dense neutral gas serves much influence on the energy loss of the plasma and disturb the increase of the electron temperature. The energy confinement time which is roughly estimated from the equation

$$\tau_E = \frac{\int \frac{3}{2}nkT dV}{P_{\text{rf}}} \simeq \frac{\frac{3}{2}\langle n_e \rangle k \langle T_e \rangle V}{P_{\text{rf}}} \quad (4.4)$$

is the order of 10^{-6} sec. This corresponds to the collision time of the electron with the neutral gas molecule. If the confinement time is determined by the diffusion of the electron through the collision with the neutral gas, the calculated confinement time is about 10sec, which is too long compared with the experimental result. Thus plasma is assumed to be lost by a recombination reaction. If the full ionization is achieved, the electron-electron or electron-ion collision becomes to be dominant and the increase of electron temperature is expected. So the effective way for the achievement of full ionization and further increase in the electron density is need to be studied.

4.3 Experiments of X-mode Wave Injection

All results described above are that of experiments with the injection of O-mode microwave, of which electric field is parallel to the magnetic field. X-mode waves, of which electric field is perpendicular to the magnetic field, has quite different property in its propagation and damping [10]. Some experiments with X-mode injection with the supported internal coil have also been carried out. In this section

the results of them is reviewed.

Figure 4.23 and 4.24 are the profile of electron density and temperature with X-mode injection measured by triple probe. In these figure the result of O-mode injection is also plotted for comparison. Both experiment have been carried out under the following condition : ECH power is $\sim 2.5\text{kW}$, neutral gas pressure is $4.0 \times 10^{-2}\text{Pa}$. It is apparent from the figure that there are no distinctive difference between the both results. The reason is assumed to be the poor absorption efficiency of incident microwave power at the ECR layer. Then the wave power is absorbed gradually through a number of reflection accompanied with the change of polarization, and polarization of the incident wave has much less effect. The rough estimation of the absorption coefficient of the incident wave at the ECR layer will be described in Sec.5.1.2.

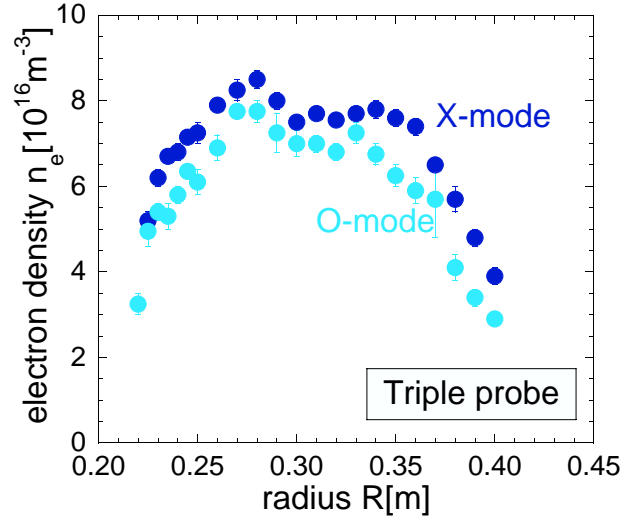


Figure 4.23: Profile of electron density with X-mode injection measured by triple probe.

The internal coil was supported when the measurement was carried out. The result of O-mode injection is also plotted for comparison. The power of microwave is $\sim 2.5\text{kW}$, and base pressure is $4.0 \times 10^{-2}\text{Pa}$ in both cases.

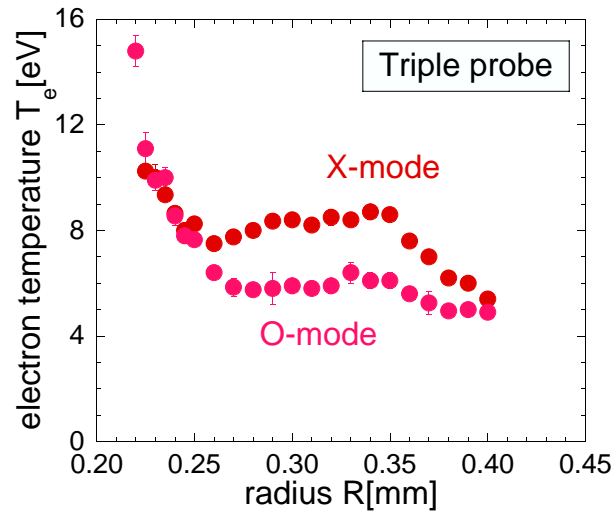


Figure 4.24: Profile of electron temperature with X-mode injection. The experimental condition is the same as described in Fig.4.23.

Chapter 5

ECH Plasma Properties

In the Mini-RT device, plasma is produced by electron cyclotron heating (ECH) at the 875G magnetic surface with a 2.45GHz microwave. In this chapter the basic physics of the ECH is reviewed and rough estimation of the absorption coefficient of the incident wave in the Mini-RT device is carried out. The application of electron Bernstein waves (EBWs), which is expected to be an effective plasma heating method in a low magnetic field, low temperature device, on the Mini-RT device is also considered in this chapter.

5.1 Physics of Electron Cyclotron Heating

5.1.1 Resonant Condition

Electron cyclotron heating (ECH) is a method of plasma heating by using electron cyclotron resonance (ECR), which is a resonant interaction between electrons and electromagnetic waves at the electron cyclotron frequency or its harmonics. ECH can be realized when injected electromagnetic wave reaches the ECR layer, where the electron cyclotron frequency Ω_e coincides with the injected wave frequency ω .

It must be noted that not all electrons can receive energy from the wave. The resonant condition is given by

$$\omega - k_{\parallel} v_{\parallel} = n \frac{\Omega_e}{\gamma} \quad (n = 1, 2, \dots) \quad (5.1)$$

where k_{\parallel} is the component of the wave number of the incident wave along the direction of magnetic field, v_{\parallel} is the component of the resonant electron velocity along the direction of magnetic field, and $\gamma = \frac{1}{\sqrt{1 - (v/c)^2}}$ is the relativistic factor of the resonant electron.

The mechanism of cyclotron resonance at the fundamental frequency ($\omega = \Omega_e$) by an X-mode wave can be easily understood. The electric field vector \mathbf{E} can be written by using two components of polarization. One description is obtained by using two linear polarizations that are perpendicular to the wave vector \mathbf{k} and perpendicular to each other (i.e. let the direction of \mathbf{k} is along the z -axis, two linear polarization is written by E_x and E_y). The other description uses two circular polarization that rotates clockwise (right-hand) or counterclockwise (left-hand) around the axis along the direction of \mathbf{k} . While the electron in the magnetic field rotates right-hand direction around the magnetic field with the cyclotron frequency due to the Larmor motion. So the electron is always accelerated under the existence of the right-hand polarized wave which propagates perpendicular direction with the same frequency. This explanation is quite simple and clear. However, ECR can be occurred by a purely O-mode wave and even by a left-hand polarized wave. In addition, above explanation cannot describe the ECR at high harmonics. To comprehend these phenomena, the consideration of the finite temperature effect of the electrons is needed.

Suppose the static magnetic field exists along the z -direction $\mathbf{B}_0 = B_0 \hat{z}$. Then equation of motion of an electron with the existence of electromagnetic wave can

be written in the form

$$\frac{d(m\gamma\mathbf{v})}{dt} = -e \left\{ \tilde{\mathbf{E}} + \mathbf{v} \times (\tilde{\mathbf{B}} + B_0 \hat{z}) \right\} \quad (5.2)$$

where the electromagnetic wave field is represented by

$$\tilde{\mathbf{E}} = E_1 e^{i(\mathbf{k} \cdot \mathbf{r} - \omega t)} \quad (5.3)$$

$$\tilde{\mathbf{B}} = B_1 e^{i(\mathbf{k} \cdot \mathbf{r} - \omega t)} \quad (5.4)$$

$$\mathbf{k} = k_\perp \hat{x} + k_\parallel \hat{z} . \quad (5.5)$$

Note x -axis is artificially set so that the wave vector is in the x - z plane.

Let $\mathbf{r}_0(t)$, $\mathbf{v}_0(t)$ is the orbit and velocity of the electron without wave field. The x, y, z component of these vectors are given by

$$x_0 = \rho \cos(\tilde{\Omega}_e t), \quad y_0 = \rho \sin(\tilde{\Omega}_e t), \quad z_0 = v_\parallel t \quad (5.6)$$

$$v_{x0} = v_\perp \sin(\tilde{\Omega}_e t), \quad v_{y0} = v_\perp \cos(\tilde{\Omega}_e t), \quad v_{z0} = v_\parallel \quad (5.7)$$

where $\tilde{\Omega}_e = \Omega_e/\gamma$, and $\rho = v_\perp/\tilde{\Omega}_e$ is ramor radius of the electron. The orbit and velocity with the wave field is written with perturbation by the field as

$$\mathbf{r}(t) = \mathbf{r}_0(t) + \mathbf{r}_1(t), \quad \mathbf{v}(t) = \mathbf{v}_0(t) + \mathbf{v}_1(t) . \quad (5.8)$$

But assuming small perturbation compared with zeroth-order value and considering the state soon after the emergence of the perturbation, this perturbation term can be negligible. So variation in the kinetic energy of the electron W is given by

$$\begin{aligned} \frac{dW}{dt} &= \mathbf{v} \cdot \mathbf{F} \\ &= -\mathbf{v} \cdot \tilde{\mathbf{E}} \\ &= -e \mathbf{v}_0(t) \cdot E_1 e^{i\{\mathbf{k} \cdot \mathbf{r}_0(t) - \omega t\}} \end{aligned} \quad (5.9)$$

The subscript 1 of electric field E_1 is omitted in following discussion. Using the description of

$$v_{x0} = \frac{iv_\perp}{2} \left(e^{i\tilde{\Omega}_e t} - e^{-i\tilde{\Omega}_e t} \right), \quad v_{y0} = \frac{v_\perp}{2} \left(e^{i\tilde{\Omega}_e t} + e^{-i\tilde{\Omega}_e t} \right), \quad (5.10)$$

the term of $\mathbf{v}_0 \cdot \mathbf{E}$ in Eq.(5.9) can be written in the form

$$\begin{aligned}\mathbf{v}_0 \cdot \mathbf{E} &= v_{x0}E_x + v_{y0}E_y + v_{z0}E_z \\ &= iv_{\perp}(E_R e^{i\tilde{\Omega}_e t} - E_L e^{i\tilde{\Omega}_e t}) - v_{\parallel}E_{\parallel}\end{aligned}\quad (5.11)$$

where $E_R = \frac{E_x + iE_y}{2}$ and $E_L = \frac{E_x - iE_y}{2}$ are the right-hand and left-hand polarization of the wave electric field around the magnetic field. The phase of the rest term of Eq.(5.9) can be described as

$$\begin{aligned}\mathbf{k} \cdot \mathbf{r}_0(t) - \omega t &= k_{\perp}x_0 + k_{\parallel}z_0 - \omega t \\ &= k_{\perp}\rho \cos(\tilde{\Omega}_e t) + (k_{\parallel}v_{\parallel} - \omega)t\end{aligned}\quad (5.12)$$

Generally in electromagnetic mode the term $k_{\perp}\rho = \frac{k_{\perp}v_{\perp}}{\tilde{\Omega}_e} = \frac{k_{\perp}c}{\omega} \frac{v_{\perp}}{c} \frac{\omega}{\tilde{\Omega}_e}$ satisfies the condition $k_{\perp}\rho < 1$ because the refractive index term $\frac{k_{\perp}c}{\omega}$ and the term $\frac{\omega}{\tilde{\Omega}_e}$ are similarly equal to unity and the term $\frac{v_{\perp}}{c}$ is less than unity. So let $\delta = k_{\perp}\rho$, the exponential of the first term of Eq.(5.12) can be expanded by the approximation include the second-order term of δ as

$$\begin{aligned}e^{ik_{\perp}\rho \cos \tilde{\Omega}_e t} &= 1 + i\delta \cos(\tilde{\Omega}_e t) - \frac{\delta^2}{2} \cos^2(\tilde{\Omega}_e t) \\ &= \left(1 - \frac{\delta^2}{4}\right) + \frac{i\delta}{2} \left(e^{i\tilde{\Omega}_e t} + e^{-i\tilde{\Omega}_e t}\right) + \frac{i\delta^2}{8} \left(e^{2i\tilde{\Omega}_e t} + e^{-2i\tilde{\Omega}_e t}\right)\end{aligned}\quad (5.13)$$

Consequently, time variation rate of electron kinetic energy is obtained as

$$\begin{aligned}
\frac{dW}{dt} = & -iev_{\perp}E_R \left\{ \left(1 - \frac{\delta^2}{4}\right) e^{i(k_{\parallel}v_{\parallel} - \omega + \tilde{\Omega}_e)t} + \frac{i\delta}{2} \left(e^{i(k_{\parallel}v_{\parallel} - \omega + 2\tilde{\Omega}_e)t} + e^{i(k_{\parallel}v_{\parallel} - \omega)t} \right) \right. \\
& \left. + \frac{\delta^2}{8} \left(e^{i(k_{\parallel}v_{\parallel} - \omega + 3\tilde{\Omega}_e)t} + e^{i(k_{\parallel}v_{\parallel} - \omega - \tilde{\Omega}_e)t} \right) \right\} \\
& + iev_{\perp}E_L \left\{ \left(1 - \frac{\delta^2}{4}\right) e^{i(k_{\parallel}v_{\parallel} - \omega - \tilde{\Omega}_e)t} + \frac{i\delta}{2} \left(e^{i(k_{\parallel}v_{\parallel} - \omega)t} + e^{i(k_{\parallel}v_{\parallel} - \omega - 2\tilde{\Omega}_e)t} \right) \right. \\
& \left. - \frac{\delta^2}{8} \left(e^{i(k_{\parallel}v_{\parallel} - \omega + \tilde{\Omega}_e)t} + e^{i(k_{\parallel}v_{\parallel} - \omega - 3\tilde{\Omega}_e)t} \right) \right\} \\
& - e_{\parallel}v_{\parallel}E_{\parallel} \left\{ \left(1 - \frac{\delta^2}{4}\right) e^{i(k_{\parallel}v_{\parallel} - \omega)t} + \frac{i\delta}{2} \left(e^{i(k_{\parallel}v_{\parallel} - \omega + \tilde{\Omega}_e)t} + e^{i(k_{\parallel}v_{\parallel} - \omega - \tilde{\Omega}_e)t} \right) \right. \\
& \left. - \frac{\delta^2}{8} \left(e^{i(k_{\parallel}v_{\parallel} - \omega + 2\tilde{\Omega}_e)t} + e^{i(k_{\parallel}v_{\parallel} - \omega - 2\tilde{\Omega}_e)t} \right) \right\}. \tag{5.14}
\end{aligned}$$

Most of the terms in Eq.(5.14) are oscillation terms and vanishes by taking time average. The resonant interaction only occurs when the following resonant condition is satisfied:

- $\omega - k_{\parallel}v_{\parallel} = 0$: Landau resonance
- $\omega - k_{\parallel}v_{\parallel} = \frac{\Omega_e}{\gamma}$: Fundamental cyclotron resonance
- $\omega - k_{\parallel}v_{\parallel} = \frac{2\Omega_e}{\gamma}$: Second harmonic cyclotron resonance

If considering n-th order terms of δ is considered in Eq.(5.13), n-th harmonic cyclotron resonance condition can be obtained through the same scheme. Where Landau resonance is not related with ECH. If the zeroth- and first-order terms of δ are considered, the variation in the electron kinetic energy is obtained as

- Fundamental cyclotron resonance:

$$\left\langle \frac{dW}{dt} \right\rangle_{\text{FCR}} = -iev_{\perp}E_R - ei\frac{k_{\perp}\rho}{2}v_{\parallel}E_{\parallel} \tag{5.15}$$

- Second harmonic cyclotron resonance:

$$\left\langle \frac{dW}{dt} \right\rangle_{2\text{HCR}} = k_{\perp} \rho v_{\perp} E_R \quad (5.16)$$

In the case of fundamental cyclotron resonance, the first term that includes E_R is dominant. Plasma discharge by the fundamental ECR depends on the term. If the electron temperature is high enough to have considerable magnitude of the $k_{\perp} \rho$ term, fundamental ECR by O-mode wave and second harmonic ECR of X-mode wave becomes effective.

5.1.2 Absorption Coefficient

In previous section the resonant condition of ECR is reviewed. However, from the standpoint of plasma heating, the coefficient of absorption is important as well as resonant condition.

The absorption coefficient can be obtained from the energy balance equation for an inhomogeneous medium which one can derive from Maxwell's equation and Vlasov equation. The energy balance equation takes the form

$$\nabla \cdot \mathbf{S} = -\alpha |\mathbf{S}| \quad (5.17)$$

where \mathbf{S} is the power flux density and α is the absorption coefficient

$$\alpha \equiv 2\text{Im}\mathbf{k} \cdot \frac{\mathbf{S}}{|\mathbf{S}|} = 2\text{Im}\mathbf{k} \cdot \frac{\mathbf{v}_g}{|v_g|} = -2\text{Im}\mathbf{k} \cdot \frac{\partial \text{Re}\Lambda / \partial \text{Re}\mathbf{k}}{|\partial \text{Re}\Lambda / \partial \text{Re}\mathbf{k}|} \quad (5.18)$$

where Λ is the determinant of the tensor $\mathbf{\Lambda}$

$$\mathbf{\Lambda} = N^2 \left(\frac{\mathbf{k}\mathbf{k}}{k^2} - \mathbf{I} \right) + \boldsymbol{\varepsilon} \quad (5.19)$$

and $\boldsymbol{\varepsilon}$ is the dielectric tensor. So absorption coefficient α can be obtained by solving local dispersion when the dielectric tensor is known. But the limiting case of a homogeneous plasma, absorption coefficient α can be described in an easier form

$$\alpha = \varepsilon_0 \omega \frac{\tilde{\mathbf{E}}^* \cdot \boldsymbol{\varepsilon}_a \cdot \tilde{\mathbf{E}}}{|\mathbf{S}|} \quad (5.20)$$

where

$$\mathbf{S} = \mathbf{S}(\text{Re}\mathbf{k}, \omega) = \frac{1}{\mu_0} \text{Re} \left(\tilde{\mathbf{E}} \times \tilde{\mathbf{B}}^* \right) - \frac{\varepsilon_0 \omega}{2} \frac{\partial \varepsilon_{h,ij}}{\partial \text{Re}\mathbf{k}} \tilde{E}_i^* \tilde{E}_j \quad (5.21)$$

and ε_h , ε_a is Hermitian and anti-Hermitian part of the dielectric tensor.

If the propagation direction of the wave is almost perpendicular to the magnetic field to satisfy $N \cos \theta < \frac{v_{\text{th},e}}{c}$ (quasi-perpendicular propagation) and plasma density is "finite" which means $\left(\frac{\omega_{pe}}{\Omega_e} \right)^2 \gg 2 \left(\frac{v_{\text{th},e}}{c} \right)^2$, the absorption coefficients of an X- and an O-mode wave are obtained by using the approximate form of the dielectric tensor [9] as

$$\alpha_1^{(\text{X})} = B \alpha_0 \quad (5.22)$$

$$\alpha_n^{(\text{X})} = A_n \alpha_{n,0}^{(\text{X})} \text{ (for } n \geq 2) \quad (5.23)$$

$$\alpha_1^{(\text{O})} = \frac{1}{2} \text{Re} N_{\perp} \left(\frac{\omega_{pe}}{\Omega_e} \right)^2 \frac{\frac{\Omega_e}{c} \text{Im} \left(-F_{\frac{7}{2}}(z_1) \right)}{\left| 1 + \frac{1}{2} \left(\frac{\omega_{pe}}{\Omega_e} \right)^2 \text{Re} \left(F_{\frac{7}{2}}(z_1) \right) \right|} \quad (5.24)$$

$$\alpha_n^{(\text{O})} = \frac{n^{2n-1}}{2^n n!} \left\{ 1 - \left(\frac{\omega_{pe}}{n \Omega_e} \right)^2 \right\}^{n-\frac{1}{2}} \left(\frac{\omega_{pe}}{\Omega_e} \right)^2 \left(\frac{v_{\text{th},e}}{c} \right)^{2(n-1)} \frac{\Omega_e}{c} \text{Re} \left(-F_{n+\frac{5}{2}}(z_n) \right) \text{ (for } n \geq 2) \quad (5.25)$$

where

$$\alpha_0 \equiv \sqrt{2} \left(1 - \frac{\omega_{pe}^2}{2\Omega_e^2} \right)^{\frac{3}{2}} \left(\frac{\Omega_e}{\omega_{pe}} \right)^2 \left(\frac{v_{\text{th},e}}{c} \right)^2 \frac{\Omega_e}{c} \frac{-\text{Im} \left(F_{\frac{5}{2}}(z_1) \right)}{\left| F_{\frac{5}{2}}(z_1) \right|} \quad (5.26)$$

$$\begin{aligned} B &\equiv B \left(z_1, \frac{\omega_{pe}^2}{\Omega_e^2} \right) \\ &= \left| 1 - \left(\frac{\omega_{pe}}{\Omega_e} \right)^2 F_{\frac{7}{2}}(z_1) \right|^2 + \frac{4}{5} \left(\frac{\omega_{pe}}{\Omega_e} \right)^2 |z_1| \left\{ \text{Re} F_{\frac{5}{2}}(z_1) - \left(\frac{\omega_{pe}}{\Omega_e} \right)^2 \text{Re} \left(F_{\frac{5}{2}}^*(z_1) F_{\frac{7}{2}}(z_1) \right) \right\} \\ &\quad + \frac{6}{35} \left(\frac{\omega_{pe}}{\Omega_e} \right)^4 \left(z_1 \left| F_{\frac{5}{2}}(z_1) \right| \right)^2 \end{aligned} \quad (5.27)$$

$$A_n \equiv \text{Re} N_{\perp}^{2n-3} |1 + a_n|^2 b_n \quad (5.28)$$

$$\alpha_{n,0}^{(X)} \equiv \frac{n^{2n-1}}{2^n n!} \left(\frac{\omega_{pe}}{\Omega_e} \right)^2 \left(\frac{v_{th,e}}{c} \right)^{2n-2} \frac{\Omega_e}{c} \left\{ -\text{Im} F_{n+\frac{3}{2}}(z_n) \right\} \quad (5.29)$$

and

$$F_q(z) = \sum_{\nu=0}^{q-\frac{3}{2}} (-z)^\nu \frac{\Gamma(q-1-\nu)}{\Gamma(q)} + \frac{\sqrt{\pi}}{\Gamma(q)} (-z)^{q-\frac{3}{2}} \{ i\sqrt{z} Z(i\sqrt{z}) \} \quad (5.30)$$

$$z_n \equiv \left(\frac{c}{v_{th,e}} \right)^2 \frac{\omega - n\Omega_e}{\omega} \quad (5.31)$$

$$a_n = \begin{cases} \frac{\frac{1}{2} \left(\frac{\omega_{pe}}{\Omega_e} \right)^2}{3 - \left(\frac{\omega_{pe}}{\Omega_e} \right)^2 \left\{ 1 + \frac{3}{2} N_\perp^2 F_{\frac{7}{2}}(z_2) \right\}} \frac{1 + 3N_\perp^2 F_{\frac{7}{2}}(z_2)}{\left\{ 1 + \frac{3}{2} N_\perp^2 F_{\frac{7}{2}}(z_2) \right\}} & \text{for } n = 2 \\ \frac{\left(\frac{\omega_{pe}}{\Omega_e} \right)^2}{n \left\{ n^2 - 1 - \left(\frac{\omega_{pe}}{\Omega_e} \right)^2 \right\}} & \text{for } n \geq 3 \end{cases} \quad (5.32)$$

$$b_n \equiv \begin{cases} \left| 1 + \frac{1}{2} \left(\frac{\omega_{pe}}{\Omega_e} \right)^2 (1 + a_2)^2 \text{Re} \left(F_{\frac{7}{2}}(z_2) \right) \right|^{-1} & \text{for } n = 2 \\ 1 & \text{for } n \geq 3. \end{cases} \quad (5.33)$$

The $\text{Re}N_\perp$ term in Eqs.5.24 and 5.28 are given by

$$(\text{Re}N_\perp)^2 = \frac{1 - \left(\frac{\omega_{pe}}{\omega} \right)^2}{\left| 1 + \frac{1}{2} \frac{\omega_{pe}^2}{\Omega_e^2} \text{Re} \left(F_{\frac{7}{2}}(z_1) \right) \right|} \quad (5.34)$$

and

$$(\text{Re}N_\perp)^2 = \begin{cases} (\text{Re}N_{\perp,c})^2 \{ 1 - \text{Re}(b + aN_{\perp,c})^2 \} & \text{for } n = 1 \\ (\text{Re}N_{\perp,c})^2 & \text{for } n \geq 2 \end{cases} \quad (5.35)$$

where

$$\text{Re}(N_{\perp,c})^2 = 1 - \left(\frac{\omega_{pe}}{\omega} \right)^2 \frac{\omega^2 - \omega_{pe}^2}{\omega^2 - \Omega_e^2 - \omega_{pe}^2} \quad (5.36)$$

$$a = -\frac{1}{2} \left(\frac{\omega_{pe}}{\omega} \right)^2 \frac{\omega^2 - \Omega_e^2}{\omega^2 - \Omega_e^2 - \omega_{pe}^2} F_{\frac{7}{2}}(z_2) \quad (5.37)$$

$$b = -2 \left\{ 1 - \frac{\omega_{pe}^2}{\omega(\omega + \Omega_e)} \right\} a , \quad (5.38)$$

and $Z(\zeta)$ is the plasma dispersion function [10].

The absorption coefficient obtained above is still complicated. So here only rough estimation is carried out. Since in the experiment mainly O-mode injection has been carried out, here absorption coefficient of fundamental O-mode is considered. When ω_{pe} is comparable with, or somewhat smaller than Ω_e , which is much likely situation in the Mini-RT, the absorption coefficient of fundamental O-mode (Eq.(5.24)) reduce to the form

$$\alpha_1^{(O)} \approx \left(\frac{\omega_{pe}}{\Omega_e} \right)^2 \frac{\Omega_e}{c} \quad (5.39)$$

It is apparent from the definition of absorption coefficient α (Eq.(5.18)) that this coefficient is that of per unit length along the propagation. So the information of the length of ECR layer is needed to calculate practical absorption coefficient. In quasi-perpendicular propagation, the ECR layer is expanded by the relativistic effects even in only weakly relativistic plasma. The relativistic line width $\Delta\omega_n$ can be estimate by

$$\frac{\Delta\omega_n}{n\Omega_e} = c_n \left(\frac{v_{th,e}}{c} \right)^2 \quad (5.40)$$

where

$$c_n = \sqrt{\frac{\pi}{2}} \left(\frac{e}{2n+3} \right)^{n+\frac{3}{2}} (2n+3)!! \quad (5.41)$$

for O-mode. Then the practical absorption coefficient α_p can be obtained in the form

$$\alpha_p = \alpha_1^{(O)} \frac{\Delta\omega_1}{\partial\Omega_e/\partial r \Big|_{\text{ECR}}} . \quad (5.42)$$

Then using the magnetic profile of the Mini-RT and assumed the density of $n_e = 5.0 \times 10^{16} \text{m}^{-3}$, calculated absorption coefficient is only 2%. This is consistent with the expectation obtained from experimental results of X-mode injection. Conse-

quently, the effort to create high-temperature electrons is needed to achieve high absorption coefficient in the Mini-RT device.

5.2 Over-dense Plasma Production by Using Electron Bernstein Waves

5.2.1 Property of Electron Bernstein Waves

Although electron cyclotron heating is a simple and effective technique for plasma production and heating, the efficient of it becomes quite small when the electron temperature is low ($v_{\text{th},e} \ll c$). In addition, such technique which utilize an electromagnetic wave cannot be applied for the heating of overdense plasma, of which electron plasma frequency ω_{pe} is larger than the frequency of the wave ($\omega_{pe} \geq \omega$). Recently, electron Bernstein waves (EBWs) are remarked to overcome this difficulty. EBW is an electrostatic wave that discovered in the theoretical analysis by I.B.Bernstein [11]. EBW has following characteristics:

- propagates perpendicular direction to the magnetic field \mathbf{B} with large wave number vector \mathbf{k} .
- has no density limit on the propagation unlike electromagnetic waves
- has wavelength λ of the order of thermal electron ramor radius ($k\rho_e \sim 1$)
- has group velocity of the order of electron thermal velocity ($v_g \sim v_{\text{th},e}$)

Consequently, EBW has quite shorter wavelength and slower group velocity compared with that of electromagnetic waves. Although damping mechanism of EBW is cyclotron resonance absorption, which is the same as that of electromagnetic waves, the absorption coefficient within the unit length along the propagation orbit

of the wave packet is quite high even in low temperature plasma because of its slow group velocity. So almost perfect absorption is expected in relatively small device, including the Mini-RT device. In addition, EBW can propagate into overdense plasma. The devices which try to achieve high beta state, such as Spherical Torus (ST), Reversed Field Pinch (RFP), generally have relatively weak magnetic field strength and the core plasma tends to be overdense. Thus electron cyclotron heating and current drive (ECH/ECCD) by using EBW have been under intense study.

5.2.2 Mode Conversion to EBW from Electromagnetic Waves

EBW is an electrostatic wave and it cannot be generated as electromagnetic waves by generator such as electrode, gyrotron, and so on. So mode conversion from an electromagnetic wave is utilized to generate EBW. Up to now, three techniques have been proposed to generate EBW by using mode conversion process near the upper hybrid resonance (UHR) layer, where the wave frequency satisfies the condition of $\omega^2 = \omega_{pe}^2 + \Omega_e^2$:

- Launching of a slow X-mode (SX) wave from high field side (SX-B conversion)
- Obliquely launching of an O-mode wave from low field side (O-X-B conversion)
- Launching of a fast X-mode (FX) wave from low field side (FX-SX-B conversion)

Figure 5.1 shows the mode conversion mechanism of SX-B conversion. A slow X-mode wave launched from high field side propagates to the UHR layer through the ECR layer. The refractive index of X-mode wave becomes very large as the wave close to the UHR layer, and it is converted into EBW by finite temperature effect of electron [10].

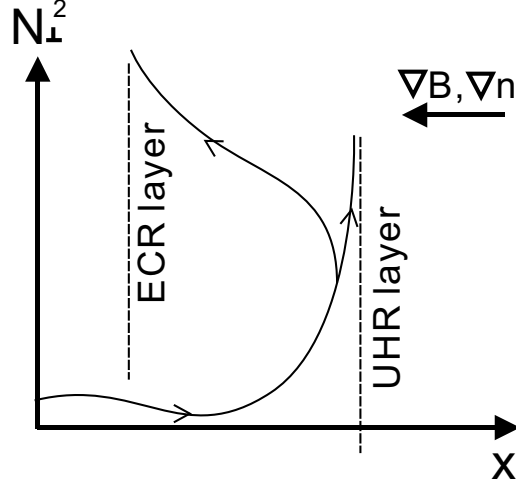


Figure 5.1: The variation in perpendicular refractive index N_{\perp} of the SX-B conversion. The curve is schematic.

Although SX-B conversion is simple and effective, launching of the wave from high field side is generally difficult due to the limited available space. (There are an interesting experiment of injecting X-mode wave from inboard side by reflecting a wave launched from outboard with using mirror and polarizer attached on the inboard vessel wall in order to avoid this difficulty [12].) In addition, an SX wave encounters left-hand cutoff (LHC) if plasma frequency is greater than twice of incident wave frequency ($\omega_{pe} \geq 2\omega$). So this technique only applicable when the peak density is less than twice of cutoff density. O-X-B conversion and FX-SX-B conversion are both launch a wave from low field side. But the condition of effective conversion is significantly different.

Figure 5.2 shows the O-X-B conversion mechanism. Generally an O-mode wave launched from low field side encounters plasma cutoff and cannot propagate further inside the plasma. But if the wave is launched with optimal angle,

$$N_{\parallel} = N_{\parallel, \text{opt}} = \sqrt{\frac{\Omega_e}{\omega + \Omega_e}} \quad (5.43)$$

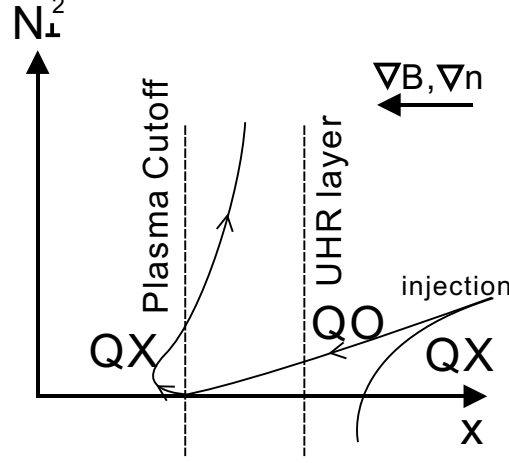


Figure 5.2: The variation in perpendicular refractive index N_{\perp} of the O-X-B conversion. The curve is schematic.

the wave is converted into an X-mode wave just at the cutoff point. The converted wave propagates backward to the UHR layer and converted into EBW as SX-B mode conversion. It is known theoretically that the efficiency of O-X-B conversion also depends the characteristic length of the density [13], which is defined as

$$L_n = \left| \frac{n_e}{dn_e/dx} \right| \quad (5.44)$$

Although experiments of heating and current drive by using O-X-B conversion has already been demonstrated in several device such as W7-AS [14], this technique has difficulty to select optimal angle. Since it is quite difficult to change the angle of the waveguide, the selection of optimal angle is generally achieved by varying the launch angle with mirror.

FX-SX-B conversion utilizes "tunneling effect" of the wave. Figure 5.3 shows this mechanism. A fast X wave launched from low field side encounters right-hand cutoff (RHC) layer before it reaches UHR layer and is reflected at the RHC layer. But if the evanescent region between RHC and UHR (Δx shown in Figure) is

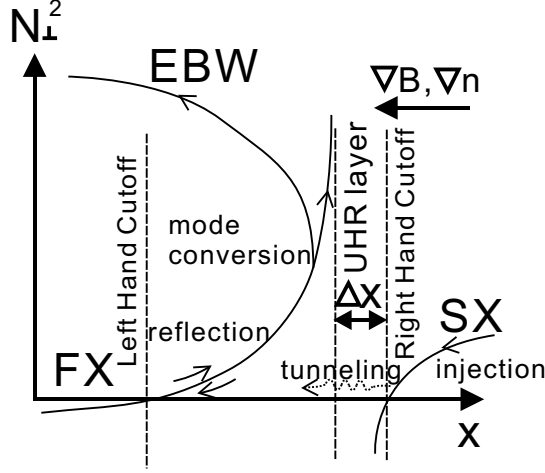


Figure 5.3: The variation in perpendicular refractive index N_{\perp} of the FX-SX-B conversion. The curve is schematic.

enough short to satisfy the condition $k_0 \Delta x \ll 1$ (k_0 is the wave number of the wave in free-space), the wave can tunnel through the region and connect the SX wave branch. Then the wave propagates inside till it reaches the LHC layer. The wave is reflected at the point and propagates backward to the UHR layer and converted into EBW. The length of evanescent region is dependent on the characteristic length of density L_n and magnetic field L_B . Generally, smaller L_n or steep density gradient is favorable to FX-SX-B conversion. So several experiments of forming artificial steep density gradient by a limiter have been carried out in NSTX (National Spherical Torus eXperiment) at Princeton Plasma Physics Laboratory (PPPL) in US [15].

Recently the new technique also has been proposed for intermediate density characteristic length [16]. This technique is combination of O-X-B conversion and FX-SX-B conversion, and high conversion efficiency is theoretically obtained in the region where both O-X-B and FX-SX-B conversion are not sufficient. Present experimental demonstration of this technique have been under intense study.

5.2.3 Application of EBW on Mini-RT experiments

The application of the mode conversion technique on the Mini-RT device has been considered. The Mini-RT device is small and the inner space of vacuum vessel is quite narrow cylindrical one whose diameter is only 0.11m. So SX-B conversion is impossible in the Mini-RT device because of insufficient space for launching. And Mini-RT device uses a 2.45GHz microwave of which launching angle cannot be changed efficiently by using a mirror. So in this study the possibility of FX-SX-B conversion in the Mini-RT device has been considered. In addition, as described in Chapter 4, the density gradient of the plasma with the levitated internal coil is very steep. So effective FX-SX-B conversion is expected in the Mini-RT device.

This is known that the conversion efficient obtained by a numerical analysis of wave equation in which finite electron temperature effect is considered coincides the absorption efficient of the X-mode wave at UHR with cold plasma approximation [10]. To utilize this fact, the efficiency of FX-SX-B conversion is analytically obtained from simple one-dimensional wave equation.

Let direction of x -axis is set to that of decreasing the magnetic field and $x = 0$ represents the point of UHR, the wave equation is described as

$$\frac{d^2 E}{d\xi^2} + \Phi(\xi)E = 0 \quad (5.45)$$

where E is the poloidal electric field, $\xi = \omega x/c$ is the normalized spatial coordinate, and Φ is a "potential function". Considered wave behavior in the vicinity of right-hand cutoff and UHR, Φ in Eq.(5.45) can be modeled by

$$\Phi(\xi) = \gamma - \frac{\beta}{\xi} \quad (5.46)$$

where $\sqrt{\gamma}$ is the normalized perpendicular wave number or the perpendicular refractive index N_{\perp} , and β/γ defines the normalized distance between right-hand cutoff and the UHR (at $\xi = 0$). This is known as Budden problem [19] and approximate

analytic solution can be obtained. Equation(5.45) is reduced in the form

$$\frac{d^2 E}{dz^2} + \left(-\frac{1}{4} - \frac{i\eta/2}{z} \right) E = 0 \quad (5.47)$$

by defining two parameters as

$$z = 2i\sqrt{\gamma}\xi, \quad \kappa = -\frac{i}{2} \frac{\beta}{\sqrt{\gamma}} \equiv -\frac{i}{2} \eta. \quad (5.48)$$

Equation(5.47) is Whittaker's equation [20]

$$\frac{d^2 E}{dz^2} + \left(-\mu^2 + \frac{\kappa}{z} \right) E = 0 \quad (5.49)$$

of $\kappa = -i\eta/2$, $\mu \pm 1/2$. The general solutions of Whittaker's equation are given by Whittaker's function $M_{\kappa,\mu}(z)$, $M_{\kappa,-\mu}(z)$, $W_{\kappa,\mu}(z)$, $W_{-\kappa,\mu}(-z)$. Since in this case 2μ is integer, the two independent solutions are given by the latter two forms. So general solution of Eq.(5.47) is given by

$$E(x) = c_1 W_{\kappa,1/2}(z) + c_2 W_{-\kappa,1/2}(-z) \quad (5.50)$$

where c_1 and c_2 are arbitrary constants that depend on the boundary conditions. Then incoming waves to the UHR and outgoing waves from the UHR are represented by approximate form of $W_{\kappa,1/2}(z)$ and $W_{-\kappa,1/2}(-z)$ in $\xi \rightarrow \pm\infty$ [17]. Assuming no damping of the wave between the UHR and LHC, difference in c_1 and c_2 can be described by phase difference ϕ as $c_2 = c_1 e^{-i(\pi+\phi)}$. Then reflection coefficient R of the incident wave at the UHR is given by

$$R = e^{-2\pi\eta} \left| 1 + e^{-i\phi} \frac{2\pi i e^{\pi\eta/2}}{\Gamma(-i\eta/2)\Gamma(1-i\eta/2)} \right|^2. \quad (5.51)$$

Using the properties of the Gamma function of $\Gamma(z+1) = z\Gamma(z)$ and $|\Gamma(-iz)|^2 = \frac{\pi}{z \sinh \pi z}$ [20], it can be shown that

$$R(\eta, \phi) = 1 - 4e^{-\pi\eta} (1 - e^{-\pi\eta}) \cos^2 \left(\frac{\phi}{2} + \theta \right) \quad (5.52)$$

where θ is the phase of $\Gamma \left(-\frac{i\eta}{2} \right)$. Now assuming no damping, conversion efficiency C is obtained by $C = 1 - R$. So maximum conversion efficiency is given by

$$C_{\max} = 4 e^{-\pi\eta} (1 - e^{-\pi\eta}) . \quad (5.53)$$

Equation (5.53) means $e^{-\pi\eta} = 0.5$ or $\eta \approx 0.22$ gives the 100% conversion. η represents the production of wave number in free-space and length between UHR and RHC $k_0 \Delta x$, and can be written by using parameters related the density and magnetic field strength around the UHR, that is

$$\eta = \frac{\Omega_e L_n}{c} \frac{\alpha}{\sqrt{\alpha^2 + 2(L_n/L_B)}} \left(\frac{\sqrt{1 + \alpha^2} - 1}{\alpha^2 + (L_n/L_B)\sqrt{1 + \alpha^2}} \right)^{1/2} . \quad (5.54)$$

where $\alpha = \left| \frac{\omega_{pe}}{\Omega_e} \right|$ and $L_B = \frac{B}{|dB/dx|}$ around the UHR.

In general $\alpha \sim 1$ is satisfied because the electron cyclotron frequency Ω_e is close to the plasma frequency ω_{pe} around the UHR layer. And in most devices the characteristic length of magnetic field is much longer than that of density ($L_B \gg L_n$). So neglecting the term L_n/L_B in Eq.(5.54), the condition that gives the perfect conversion is obtained as

$$|BL_n|_{\text{UHR}} = 1.5 \times 10^{-4} [\text{T} \cdot \text{m}] . \quad (5.55)$$

This result shows that very short L_n or steep density gradient is needed for conversion with high efficiency : 1.5mm for 0.1T, 0.15mm for 1T.

The Mini-RT device has relatively low magnetic field strength and steep density gradient. So condition of Eq.(5.55) is favorable. However, the Mini-RT device has dipole magnetic field and the magnetic field gradient is comparable to the density gradient. So it is needed to calculate the conversion efficiency with original equation Eq.(5.54) . Figure 5.4 shows the position of UHR and RHC layer on the equatorial plane of the Mini-RT device. In this calculation, magnetic field and density profile are given by using the fitting function of the experimental data, which corresponds

to Fig.4.18. The calculated position of UHR corresponds to the radius of 0.26m, where the magnetic field strength is 0.022T and electron density is $6.7 \times 10^{16} \text{m}^{-3}$. The characteristic length of magnetic field and density at the point are 0.063m and 0.013m, respectively. Then maximum conversion efficiency calculated from these value by using Eq.(5.54) is 65%. Note this efficiency is theoretical maximum one and it can change by the phase of incident wave. However, compared with other experimental devices, the Mini-RT has the possibility of FX-SX-B conversion with high efficiency in its nature.

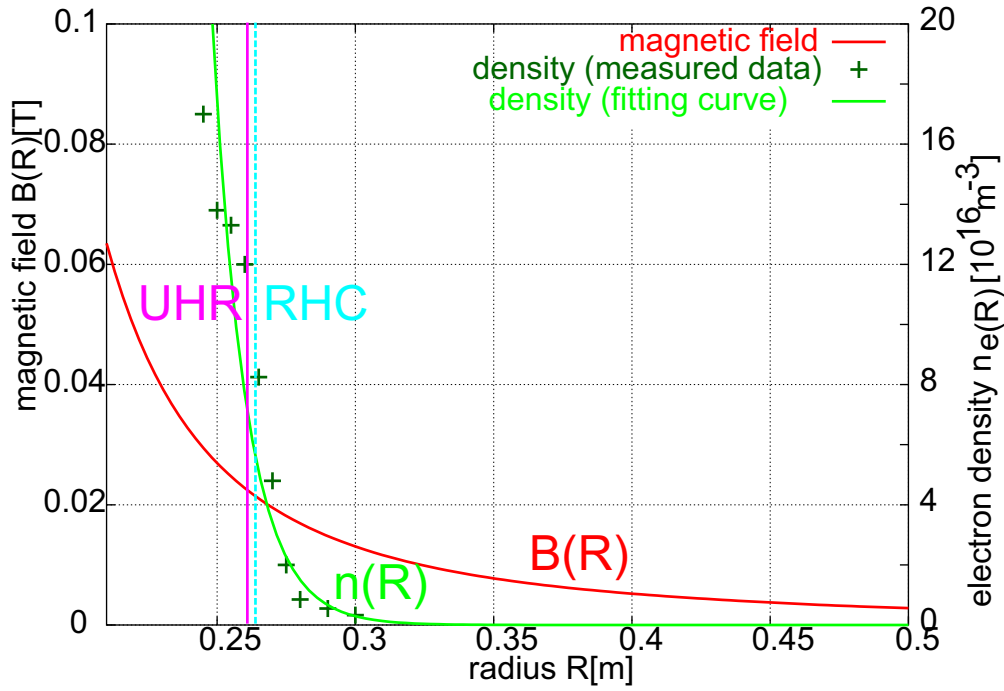


Figure 5.4: The position of upper hybrid resonance (UHR) and left-hand cutoff (LHC) in the experiment. The profiles of magnetic field and density (fitting) used in the calculation are also shown.

Chapter 6

Conclusion

The Mini-RT device is a relatively small ($R = 0.5\text{m}$) internal coil device which was constructed in order to achieve extremely high-beta plasma confinement that predicted in two fluid relaxation theory by Mahajan and Yoshida. To achieve the final goal, much effort have been being put on the establishment of experimental environment. Up to now, the environment for carrying out the experiment with the levitated internal coil have been put into the place through the first plasma experiment, energizing test of the internal coil, levitation control test of the internal coil, and the plasma production with levitated internal coil. While it is assumed that the existence of the supporting structure in the plasma can be an obstacle to the high-density and high-temperature plasma production.

Then experiments which aims the comprehension of the effects of the internal coil levitation on the plasma parameters and clarification of the physics approach to achieve high density and high temperature plasma production have been carried out. In this experiments, plasma has been produced by electron cyclotron heating (ECH) with a 2.45GHz microwave up to 3kW. The measurement of plasma parameters (i.e. electron density and temperature) has been carried out by using electrostatic probes (double and triple probe) and a 75GHz microwave interferometer.

Through the study, following facts become to be clear. First, the reliability of the conventional measurement by electrostatic probes has been verified through the cross check with the microwave interferometer. This enables the analysis of the electron density including the comparison with the cutoff density of 2.45GHz microwave ($7.4 \times 10^{16} \text{m}^{-3}$). Second, the levitation of the internal coil (i.e. the removal of the supporting structure from plasma region) enables the plasma production with low neutral gas pressure below $1 \times 10^{-2} \text{Pa}$, which cannot be achieved in the past experiments with the supported internal coil. With about 25mm levitation of the internal coil and 20mm descending of the supporting structure, plasma production in the condition that neutral gas pressure is $1.2 \times 10^{-3} \text{Pa}$ have been achieved. Following this facts, the ionization degree has been increased from the order of 1% to 50%, which indicates that the plasma is transferring from the region in which the collision of the electron with neutral gas is dominant to the one in which the high-density, high-temperature plasma production is possible. In addition, in such low neutral gas pressure, it has been verified that the electron density and temperature are increase compared with that with supported coil. Especially, the maximum electron density measured by probes totally above (about twice of) the cutoff density. So it indicates the overdense plasma production has occurred.

According to the theoretical calculation, the absorption coefficient of the incident wave around the ECR of the Mini-RT device is quite weak ($\sim 2\%$). In fact, the experimental results of the X-mode injection has no much difference with the O-mode injection. It also indicates the absorption in one-path is not much enough. Although the ionization degree is significantly increases by the levitation of the internal coil, the confinement properties indicates the collision of electrons with the neutral gas particles is still dominant. So full ionization and further increase in the temperature is needed to achieve high beta plasma production. However, the Mini-RT device, by its nature of relatively low magnetic field ($\lesssim 0.1 \text{T}$) and the

steep density gradient which formed when the internal coil is levitated due to the separatrix, has the high possibility of the generation of electron Bernstein wave (EBW) through mode conversion of the X-mode wave launched from the outboard side. EBW has no density limit in its propagation and can be strongly damped on the electrons around the ECR even in low temperature. Although several problem remains, there is a possibility of effective heating of the plasma of Mini-RT by using EBW.

Consequently, the levitation of the internal coil has great effect on the improvement of plasma parameters. To achieve further improvement, more reliable measurement, especially electron temperature, by using other techniques and further analysis of the physics of ECH in the Mini-RT are needed.

Appendix A

Sheath Theory

It is known that the plasma near a conductor which applied negative potential V_p against space potential V_s forms three distinct region (see Fig.A.1) .

Since in plasma experiments generally plasma consists of electrons and ions of one species, the following consideration also assumes such plasma. In the region which is far from the conductor, plasma can hold the neutrality ($n_e = Z_i n_i$) . Where n_e and n_i are density of electron and ion, respectively, and Z_i is charge number of ion. The effect of the conductor potential emerges around point C and form negative electric field, which decelerates electrons and accelerates ions. But in this region quasi-neutrality remains to be hold because decrease of electrons is quite small due to the weak electric field and ions are also decreased due to the acceleration. In the region inner the B point, strong negative electric field is formed. Due to this negative field, most electrons are excluded and ion sheath is formed. It is known that the potential of the sheath edge (B point) V_0 is determined by the electron temperature as

$$V_0 = \frac{kT_e}{2e} . \quad (\text{A.1})$$

If the neutral gas density is low enough that the collision of ions with neutral particles within the region between B and C is negligible, the velocity of the ion v_i

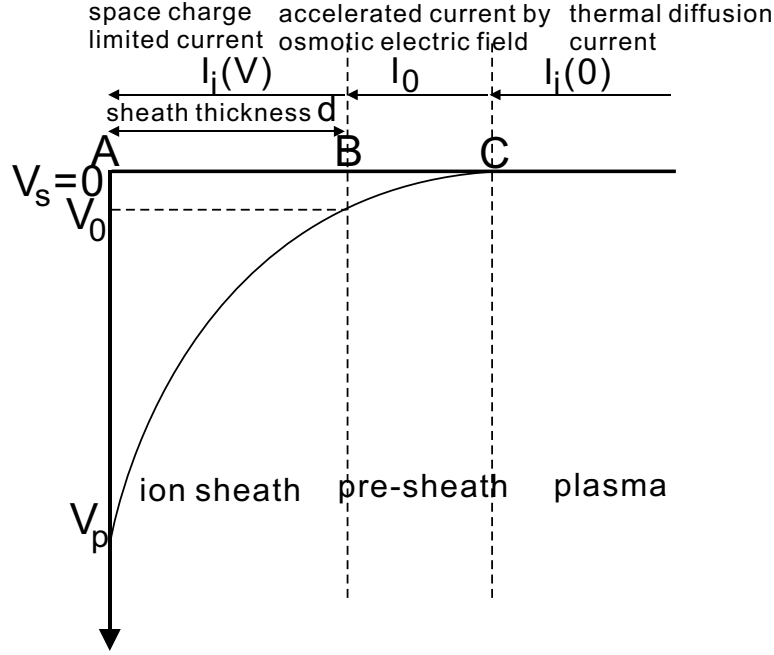


Figure A.1: Structure and potential profile of ion sheath

at the sheath edge is determined by V_0 or T_e as

$$v_i = \sqrt{\frac{2eV_0}{m_i}} = \sqrt{\frac{kT_e}{m_i}} . \quad (\text{A.2})$$

While current flowing into sheath edge which accelerated by osmotic electric field I_0 is given by

$$I_0 = n_i(V_0)ev_iS \quad (\text{A.3})$$

where $n_i(V_0)$ is the ion density at sheath edge, S is the surface area of ion sheath. Assuming the electron energy is determined by maxwell distribution, electron density at sheath edge $n_e(V_0)$ can be described by the electron density of the plasma region as

$$n_e(V_0) = n_e(0) \exp\left(-\frac{eV_0}{kT_e}\right) = 0.61n_e(0) . \quad (\text{A.4})$$

Since quasi-neutrality is still kept at sheath edge, $n_i(V_0) \simeq n_e(V_0)$ is satisfied. While $n_e(0) = n_i(0)$ is satisfied in the plasma region. This yields the equality $n_i(V_0) = 0.61n_i(0)$. So using Eqs.(A.2) and (A.3), we can obtain

$$I_0 = 0.61n_i(0)e\sqrt{\frac{kT_e}{m_i}}S . \quad (\text{A.5})$$

This gives the equation of the saturation current of double probe (Eq.(3.2)) .

The current flowing into the sheath edge I_0 is continuously accelerated and flows into the conductor. Since in the sheath region most particles are ion, the current is limited by the space charge. The amount of the space charge limited current is determined by solving Poisson equation and it is given as the Langmuir-Child's law [8] which can be written in the form

$$I_i(V) = \frac{4\varepsilon_0}{9} \sqrt{\frac{2e}{m_i}} \frac{(V_p - V_0)^{\frac{3}{2}}}{d^2} . \quad (\text{A.6})$$

where d is the thickness of the ion sheath. This current must be equal to the saturation current which given by Eq.(A.5). The sheath thickness d increases as the potential V_p is increasing. It is proportional to $V_p^{\frac{3}{2}}$ with the constant n_e and T_e . For this reason the current of double probe is saturated at the high probe voltage. However, in the probe measurement, the size of the conductor is infinite. So the shape of the sheath is not the ideal strati-form as considered above due to the edge effect. Especially, if the shape of the conductor is not plane, the effective surface area of the conductor increases as the increase of the sheath thickness. Several analysis including consideration of these effect have been carried out by using the approximate solution of the Poisson equation. According to these analysis, the space charge limited current is given by replacing d^2 in Eq.(A.6) of

$$r_p^2(\gamma^2 + 0.6\gamma^3 + 0.24\gamma^4 + 0.074\gamma^5 + \dots) \quad (\text{A.7})$$

for spherical conductor and

$$r_p^2(\gamma + 0.4\gamma^2 + 0.09167\gamma^3 + 0.01424\gamma^4 + \dots)^2 \quad (\text{A.8})$$

for cylindrical conductor. Where $\gamma = \frac{r_s}{r_p}$ and r_s, r_p are the radius of ion sheath and conductor, respectively. It is possible to calculate the radius of ion sheath from this equation and estimate the effective surface area of the probe. But in the calculation the information of the electron density, the electron temperature, and the probe potential are needed. Since these values are unknown in experiments, the accurate estimation of the electron temperature and density including the effective increase of the probe surface area from the data measured by the probe needs numerical calculation with iterations.

Appendix B

High Energy Electron Loss by the Support Structure

As mentioned in Sec.4.2, when the internal coil is supported, the electron density decreases as the neutral gas pressure is decrease, and plasma production becomes impossible at the neutral pressure of less than 1×10^{-2} Pa. Here one assumption that can explain this phenomenon is introduced.

Although it is not measured experimentally, the electric field in the Mini-RT device is assumed to be negligible. So the component of the guiding center velocity of plasma which is particle perpendicular to the magnetic field $\mathbf{v}_{g\perp}$ is probably determined by the ∇B drift velocity

$$\mathbf{v}_{\nabla B} = \frac{W_{\perp} \mathbf{B} \times \nabla B}{qB^2} = \frac{\frac{1}{2}mv_{\perp}^2 \mathbf{B} \times \nabla B}{qB^2} . \quad (\text{B.1})$$

Since $v_{\perp} \approx v_{\text{th},e}$ is assumed for electrons, the ∇B drift velocity can be written in the form

$$v_{\nabla B} = \frac{\frac{1}{2}m_e v_{\text{th},e}^2}{eBL} = \frac{T_e}{BL} \quad (\text{B.2})$$

where T_e is in eV, and $L = \left| \frac{B}{\nabla B} \right|$.

The collision cross-section of a electron for the ionization of H_2 gas σ_{en} is the function of the electron energy, and it has maximum for the electron of which temperature is around 100eV [21] (see Fig.B.1). So here the electron with the temperature of 100eV, which has the thermal velocity of $v_{th,e} = 7.26 \times 10^6$ m/sec, is considered. Since the magnetic field strength B and characteristic length L in the measurement of the neutral pressure dependence of the electron density are 0.04T and 0.1m, respectively, the ∇B drift velocity of the electron is $v_{\nabla B} = 4 \times 10^4$ m/sec. The collision cross-section for ionization of the electron σ_{en} with the temperature of 100eV is known to be 9×10^{-21} m² by experimental measurements. So the collision time τ_{en} and mean free path $\lambda_{en} = v_{th,e}\tau_{en}$ of the electron in the H_2 gas of 4.0×10^{-2} Pa, which corresponds to the neutral density of 8×10^{18} m⁻³, are 2×10^{-6} sec and 14m, respectively. Since the number of the support structure is three and they locate equiangularly on the radius of $R = 0.25$ m, the maximum distance between them is $2 \times 0.25\pi/3 = 0.42$ m. Then the time within which the electron collide with the support structure by ∇B drift is 2×10^{-5} sec at maximum. Since it is assumed the parallel component of the electron velocity v_{\parallel} is almost equal to the thermal velocity, the electron moves 140m during the time. Therefore, the electron collides averagely with 10 neutral gas molecules and ionizes them before it collides with the support structure and is lost. If the neutral gas pressure becomes less than 4×10^{-3} Pa, the electron is lost before it ionize neutral gas molecules, which means the disability of plasma production. This value agrees in the order with the experimental results.

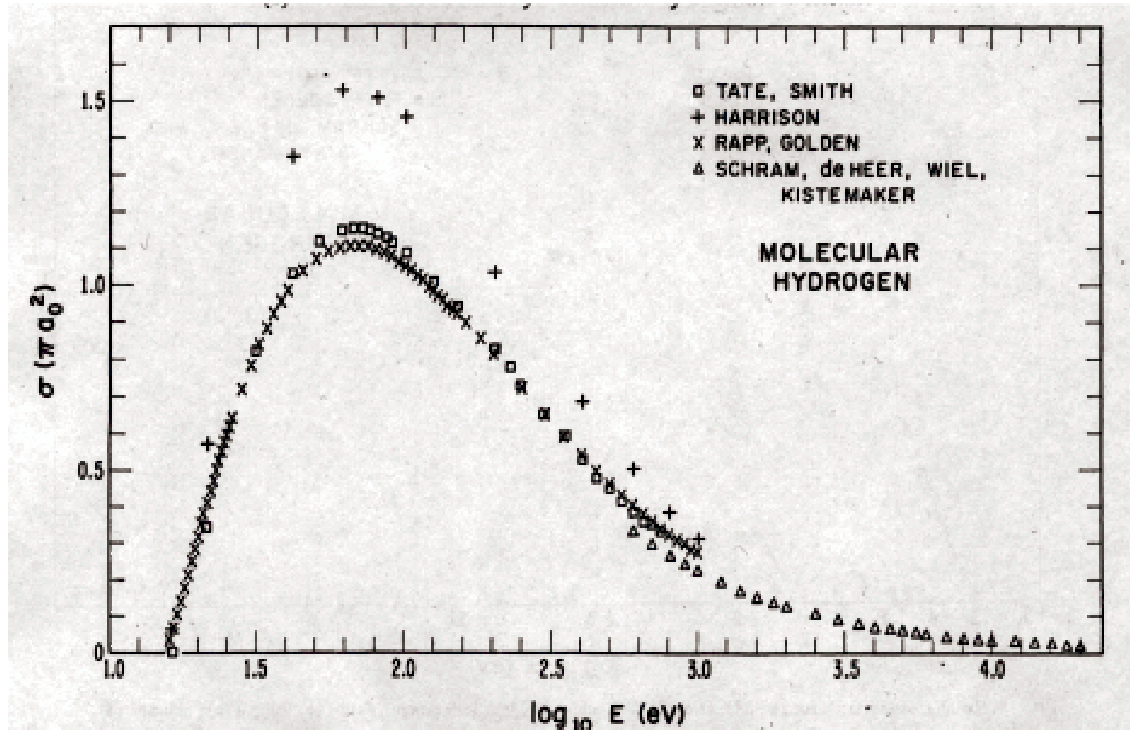


Figure B.1: Total cross sections for the ionization of molecular hydrogen [21]. The cross-section of the vertical axis is normalized by $\pi a_0^2 (= 8.797 \times 10^{-21} \text{m}^2)$, where a_0 is Bohr radius.

Acknowledgment

I am greatly appreciate the help and kindness of the member of Ogawa laboratory and Yoshida-Himura laboratory provided in this investigation.

First of all, I am profoundly grateful to Professor Yuichi Ogawa, my direct supervisor. He kindly takes time from his busy schedule to discuss with me, and give precise instructions and valuable advices. I also acknowledge Professor Zensho Yoshida and Professor Haruhiko Himura for their pointed indications.

I also appreciate for the member of the Mini-RT experimental group in proceeding experiments. Mr. Junji Morikawa kindly teaches knowledge and skills of plasma experiment and measurement. I could not carried out the experiments without his help. Mr. Eiichi Yatsuka always assist me in experiments and discussions with him are very constructive. Mr. Dan Hori, Mr. Shigeo Yamakoshi and Mr. Kotaro Ohkuni have worked hard to establish the experimental environment in early phase of Mini-RT program. And many members of private companies (Vega Technology Co. , Sanyu Engineering Co. , Cryovac Co. , JECC Torisha Co. also help to fix up the experimental equipments.

I also grateful to the member of experimental group of the laboratory, Mr. Haruhiko Saito, Mr. Hidenori Wakabayashi, Mr. Tomonari Kurihara, Mr. Sho Watanabe and Mr. Atsushi Wada. Especially, Mr. Saito give very helpful advices about the interpretation of experimental results. And Mr. Watanabe often helps me in the daily life as a contemporary and his attitude on his work always impresses me. And I also ap-

preciate for the member of theoretical group of the laboratory, Dr. Shuichi Ohsaki, Dr. Masaru Furukawa, Mr. Makoto Hirota, Mr. Jun-ya Shiraishi, and Mr. Shuhei Numazawa. They kindly advise me despite there were not so much chance for discussion.

And I give thanks to Ms. Machiko Yutani and Ms. Nami Tonegawa for their heartily support in daily life.

Last of all, I really appreciate my parents and loved wife to provide me emotional support.

Bibliography

- [1] F.F.Chen, "*Introduction to Plasma Physics*", Plenum Press (1974)
- [2] Many references. For example,
S.M.Krimigis *et al.*, "Hot Plasma Environment at Jupiter: Voyager 2 Results",
Science **206** 977 (1979)
- [3] A.Hasegawa *et al.*, "A D-³He Fusion Reactor Based on a Dipole Magnetic Field", Nucl. Fusion **30** 2405 (1990)
- [4] Z.Yoshida and S.M.Mahajan, "Variational Principles and Self-Organization in Two-Fluid Plasmas", Phys. Rev. Lett. **88** 095001 (2002)
- [5] S.M.Mahajan and Z.Yoshida, "Double Curl Beltrami Flow: Diamagnetic Structures", Phys. Rev. Lett. **81** 4863 (1998)
- [6] Z.Yoshida *et al.*, "Toroidal Magnetic Confinement of Non-Neutral Plasmas", Non-Neutral Plasma Physics **3** 397 (1999)
- [7] Y.Ogawa *et al.*, "Levitated Superconductor Ring Trap (Mini-RT) Project –A New Self-Organized Structure with Strong Plasma Flow–", *Proceedings in 19th IAEA Fusion Energy Conference*, Lyon, France, 14-19 October 2002 IC/P-12
- [8] I.Langmuir, "The Effect of Space Charge and Residual Gases on Thermionic Currents in High Vacuum", Phys. Rev. **2** 450 (1913)

- [9] M.Bornatici, *et al.*, "Electron cyclotron emission and absorption in fusion plasmas", Nucl. Fusion **23** 1153 (1983)
- [10] T.H.Stix, "*Waves in Plasmas*", American Institute of Physics (1992)
- [11] I.B.Bernstein, "Waves in a Plasma in a Magnetic Field", Phys. Rev. **109** 10 (1958)
- [12] T.Maekawa *et al.*, "Doppler-Shifted Cyclotron Absorption of Electron Bernstein Waves via N_{\parallel} -Upshift in a Tokamak Plasma", Phys. Rev. Lett. **86** 3783 (2001)
- [13] E.Mjølhus, "Coupling to Z mode near critical angle", J. Plasma Phys. **31** 7 (1984)
- [14] H.P.Laqua *et al.*, "Resonant and Nonresonant Electron Cyclotron Heating at Densities above the Plasma Cutoff by O-X-B Mode Conversion at the W7-As Stellarator", Phys. Rev. Lett. **78** 3467 (1997)
- [15] G.Taylor *et al.*, "Enhanced conversion of thermal electron Bernstein waves to the extraordinary electromagnetic mode on the National Spherical Torus Experiment", Phys. Plasmas **10** 1395 (2003)
- [16] H.Igami, *et al.*, "Polarization adjustment of incident electromagnetic waves for optimal mode-conversion to electron Bernstein waves", Plasma Phys. Control. Fusion **46** 261 (2004)
- [17] A.K.Ram, A.Bers, and S.D.Shultz, "Mode conversion of fast Alfvén waves at the ion-ion hybrid resonance", Phys. Plasmas **3** 1976 (1996)
- [18] A.K.Ram *et al.*, "Excitation, propagation, and damping of electron Bernstein waves in tokamaks", Phys. Plasmas **7** 4084 (2000)

- [19] K.G.Budden, ” *The Propagation of Radio Waves*”, Cambridge University Press (1985)
- [20] M.Abramowitz and I.A.Stegun, ” *Handbook of Mathematical Functions*”, Dover (1970)
- [21] L.J.Kieffer and G.H.Dunn, ”Electron Impact Ionization Cross-Section Data for Atoms, Atomic Ions, and Diatomic Molecules: I. Experimental Data”, Rev. Mod. Phys. **38** 1 (1966)

Related Presentation

- T.Goto, K.Ohkuni, S.Yamakoshi, K.Ichikawa, J.Morikawa and Y.Ogawa
"ECH plasma experiments of the internal coil device Mini-RT"
5th Fusion Energy Collaboration Meeting, Sendai, Japan, 17-18 June 2004
- T.Goto, E.Yatsuka, J.Morikawa, Y.Ogawa and N.Yanagi
"ECH Plasma Experiments on the Internal Coil Device Mini-RT (III)"
JPS Autumn Meeting, Aomori, Japan, 12-15 September 2004
- T.Goto, E.Yatsuka, J.Morikawa, Y.Ogawa and N.Yanagi
"ECH plasma properties of the internal coil device Mini-RT"
JSPF Annual Meeting, Sizuoka, Japan, 23-26 November 2004